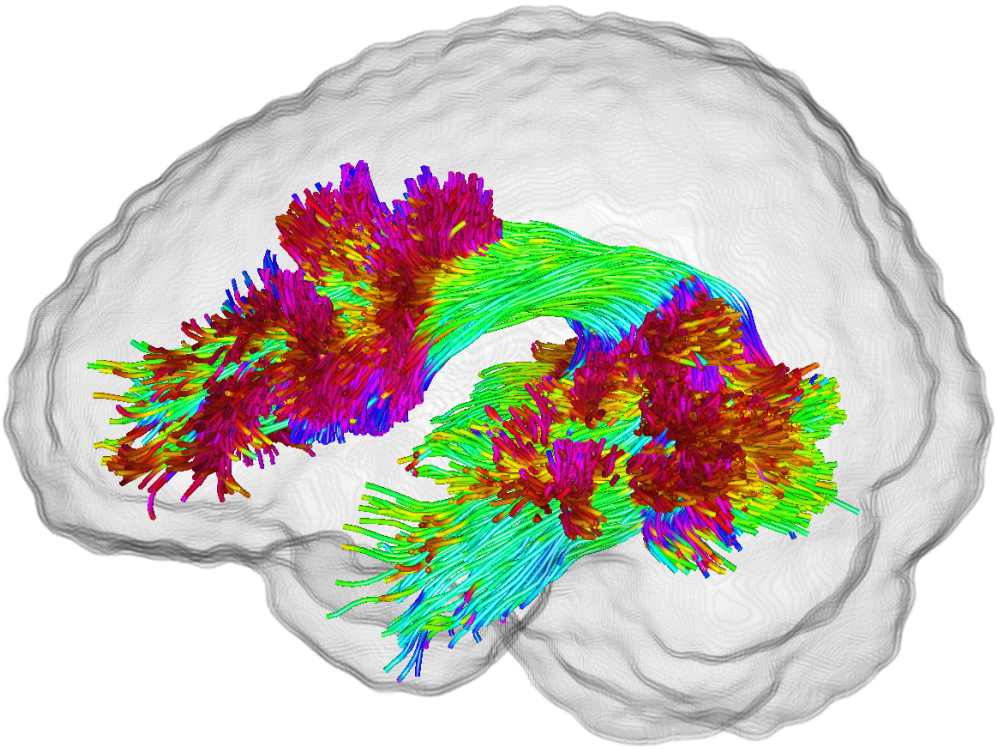

DWI Pre-Processing, Tractography and Analysis for Glioma Patients

Master's thesis in Biomedical Engineering

ELINA PETERSSON

DEPARTMENT OF ELECTRICAL ENGINEERING

CHALMERS UNIVERSITY OF TECHNOLOGY
Gothenburg, Sweden 2023
www.chalmers.se

Master's thesis 2023

DWI Pre-Processing, Tractography and Analysis for Glioma Patients

ELINA PETERSSON

UNIVERSITY OF
GOTHENBURG

CHALMERS
UNIVERSITY OF TECHNOLOGY

Department of Electrical Engineering
Chalmers University of Technology
University of Gothenburg
Gothenburg, Sweden 2023

DWI Pre-Processing, Tractography and Analysis for Glioma Patients
ELINA PETERSSON

Supervisor: Alice Neimantaite, University of Gothenburg
Examiner and Chalmers supervisor: Ida Häggström, Department of Electrical Engineering, Chalmers University of Technology

Master's Thesis 2023
Department of Electrical Engineering
Chalmers University of Technology and University of Gothenburg
SE-412 96 Gothenburg
Telephone +46 31 772 1000

Cover: left arcuate fasciculus visualization in Slicer 3D.

Typeset in LaTeX
Printed by Chalmers Reproservice
Gothenburg, Sweden 2023

Abstract

Background and purpose: Glioma is the most common type of brain tumor, and there is a continuous need for research on the relations between glioma related effects on the brain and patient health related quality of life. Brain imaging gives the potential to investigate changes in the brain. This thesis aims to facilitate the future work of a research group at Sahlgrenska University Hospital by developing a workflow including pre-processing of diffusion-weighted magnetic resonance images (DWI), performing tractography, and analyzing the resulting brain tracts.

Methods: The open-source white matter segmentation tool TractSeg was applied after image pre-processing steps including removal of noise, Gibbs ringing artifacts, susceptibility-induced distortions, eddy currents, motion artifacts, and bias fields, as well as registration to MNI space. Tract approximations of 16 glioma patients were compared to those of 42 healthy subjects from the Human Connectome Project using TractSeg's Tractometry module. The comparison was based on fractional anisotropy and fiber orientation distribution peak length.

Results: TractSeg successfully computed 99.0% of the tracts for the 16 glioma patients and demonstrated indications of ability to handle the skewed brain anatomies observed in glioma patients. The comparison of fractional anisotropy between patients and healthy subjects revealed that the most affected brain tracts in the cohort were the anterior thalamic radiation, corpus callosum, cingulum, and striato-fronto-orbital tract. The comparison based on peak length indicated the most affected tracts to be the anterior thalamic radiation, corpus callosum, striato-fronto-orbital, thalamic-premotor, and thalamo-parietal tract.

Conclusions: The most affected brain tracts, as determined by fractional anisotropy and peak length comparison, were mostly located in the frontal lobe, which is consistent with previous findings related to glioma localization. TractSeg exhibits potential for performing tractography on glioma patient images and generating accurate tract approximations. The absence of ground control brain tract outlining poses challenges in quantitatively evaluating TractSeg performance on glioma-induced shifted brain anatomy and the following tract analysis. To enable future research, it is advisable to conduct a comparison with a control method to evaluate the performance of TractSeg.

Keywords: tractography, glioma, diffusion-weighted imaging, pre-processing, constrained spherical deconvolution, TractSeg

Acknowledgements

This project has been done under the supervision of doctoral student Alice Neimantaite in the research group Clinical Brain Tumor Research at the University of Gothenburg. Thank you to Alice Neimantaite, who has been of great support throughout the process of this project. Furthermore, thank you to the people of the research group who kindly welcomed me to the office, and helped me with all kinds of inquiries.

MR images from brain tumor patients were collected at Sahlgrenska University hospital.

Data representing healthy population were provided by the Human Connectome Project, WU-Minn Consortium (Principal Investigators: David Van Essen and Kamil Ugurbil; 1U54MH091657) funded by the 16 NIH Institutes and Centers that support the NIH Blueprint for Neuroscience Research; and by the McDonnell Center for Systems Neuroscience at Washington University.

Acronyms

CSD - Constrained spherical devonvolution

DTI - Diffusion tensor imaging

DWI - Diffusion-weighted imaging

FA - Fractional anisotropy

FOD - Fiber Orientation Distribution

HCP - Human Connectome Project

MNI - Montreal Neurological Institute (standard space)

MRI - Magnetic Resonance Imaging

TOM - Tract Orientation Map

Contents

1

Introduction

Glioma is the most common type of malignant brain tumor, accounting for around 30% of all tumors in the central nervous system [1]. 15% of the gliomas are low-grade gliomas, affecting 1 per 100 000 persons each year, and are characterized by slow-growing tumors that eventually become more aggressive and lead to death [2]. The clinical care process for gliomas is illustrated in Figure 1.1, and is most often initiated due to some tumor symptom. The most common tumor symptom is new-onset epileptic seizures [3], but can also be fatigue, headache, or vision loss [4]. A proportion of tumor patients are discovered incidentally, for example when they undergo a magnetic resonance imaging (MRI) session due to reasons not related to the tumor, and the tumor is detected [3].

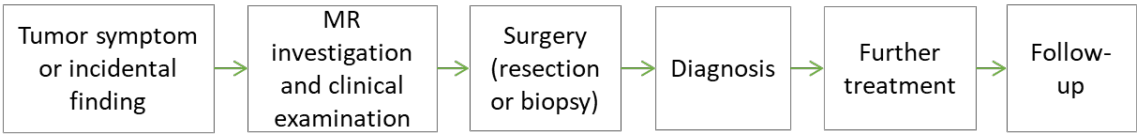

Figure 1.1: Flow chart of the clinical care workflow.

Typically clinical examination and brain MRI are used to form an initial treatment plan, which normally starts with surgery, and further treatment consists of a combination of radiotherapy and chemotherapy [4]. Through a biopsy taken during surgery, often in conjunction with tumor resection (surgical removal of the tumor), a molecular diagnosis of the tumor is made [4]. Moreover, the patients will regularly undergo follow-ups in terms of MRI after treatment since gliomas are non-curable [5].

Although diagnosed patients can now survive longer because of advancements in treatment, there are potential negative outcomes after surgery, such as sustained cognitive, emotional, and social function impairment [6]. How the impairments are related to tumor properties, tumor effect on the brain, and treatment is however not clear. Additionally, the slow growth of low-grade gliomas could induce brain plasticity, i.e., the ability of the brain to re-organize and move functions to different locations. However, it still remains to be investigated to what extent brain plasticity occurs in glioma patients and how it is connected to patients' health-related quality of life.

1.1 Aims and objectives

This thesis is part of a research project at Sahlgrenska University Hospital that studies how clinical and imaging data, including tumor properties and anatomical and functional changes in the brain, are related to glioma patients' cognitive function and quality of life. One area of interest for the research project is to study white matter brain tracts of glioma patients to acquire further knowledge on gliomas and the treatment of gliomas. To enable the future work of the research project, this thesis aims to make preparatory work in terms of processing and analyzing diffusion-weighted MR images, for the purpose to investigate brain tract health and changes.

The objective of this thesis is to establish an automatic image-processing workflow to obtain nerve tract approximations from diffusion-weighted MR images from glioma patients. The workflow will be based on already existing functions and tools and consist of pre-processing steps to correct for image artifacts before performing tractography that outputs 2D and 3D images of the brain tracts. The resulting images will be further analyzed to investigate the properties of glioma patients' brains. Questions to investigate in the project are: how are the tracts of the patients in the cohort affected by the gliomas? Are some tracts affected more than others? Which methods are most suitable for the analysis of the tracts?

2

Theory

The theoretical background to the project includes basics on the anatomy of the brain and its white matter tracts, followed by the steps needed for imaging the tracts using magnetic resonance imaging and a description of how the tracts can be analyzed.

2.1 Anatomy of the brain

The brain consists of nerve cells, called neurons, and different types of glial cells. Glial cells provide support to the neurons in terms of for example supplying nutrients, repairing, making myelin, and immune defense. The cell bodies of the neurons, see Figure 2.1, mainly contain water and constitute what is called the gray matter of the brain. Axons are outgrowths of the neurons that transmit signals, and they are covered in fatty sheaths called myelin to increase the speed of signal transduction. The myelinated axons make up the white matter of the brain [7].

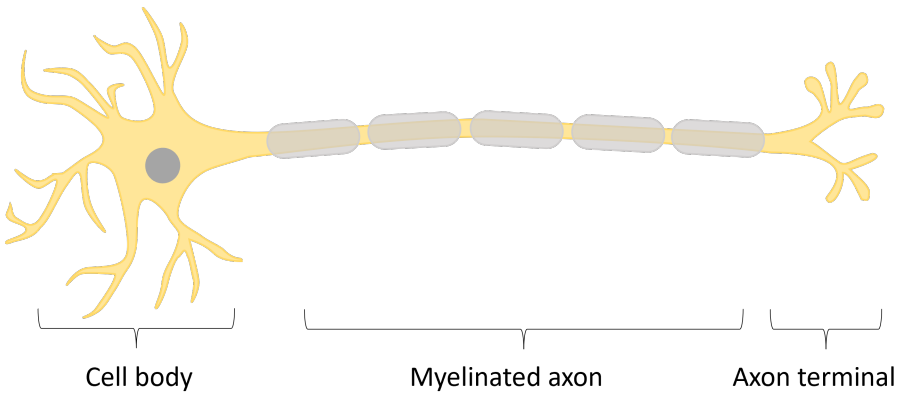

Figure 2.1: Drawing of a neuron.

2.1.1 Brain tracts

Brain tracts, or fasciculi, are bundles of axons that send information between different areas of the brain. Cell bodies of neurons that are close to each other and have similar connections in the brain are grouped into nuclei. The cell bodies in a nucleus are connected to other neurons via their axons and since the axons of a

nucleus tend to go along a similar route, they naturally form bundles that connect nuclei of different locations in the brain, and those bundles are called tracts [7]. A smaller bundle of axons can be called a fiber and therefore, a tract can also be termed a bundle of fibers. The tracts can be seen as neural highways going from one area in the brain to another and the brain contains an intricate network of tracts enabling all necessary functions that the brain supplies.

Classification of the tracts can be done into association fibers, commissural fibers, and projection fibers. There are short association fibers, also called U fibers, that connect neighboring areas of the brain, and long association fibers that connect areas further away within the same hemisphere. Depending on how the tracts are distinguished, e.g., by dissection or imaging, there are different ways to classify the tracts to either belong to the association, commissural, or projection fibers [8]. Table A.1 in Appendix A displays tracts according to how the open-source white matter segmentation tool TractSeg[9] classifies them, which will be the classification used in this project.

The association fibers include for example the superior longitudinal fascicle, cingulum, and arcuate fascicle (see Figure 2.2). Opposed to the association fibers that connect areas within one hemisphere, the commissural fibers form bridges between the two hemispheres, of which the most important tract is the corpus callosum. The projection fibers connect the cerebral cortex to structures below, such as the spinal cord. Examples of projection fibers include the corticospinal tract and optic radiation (see Figure 2.2). Moreover, all the tracts connect different areas of the brain and can hence be related to different functions, e.g., the superior longitudinal fascicle transmits signals related to many cognitive functions such as memory, emotions, and language, and the arcuate fascicle is involved in processing language. The corticospinal tract connects the motor cortex to the spinal cord and is hence imperative for motor control, while the optic radiation makes sure signals from the optic nerve are sent to the visual cortex in the occipital lobe [10].

2.2 Diffusion weighted imaging

The imaging modality considered in the project, diffusion-weighted imaging (DWI), is a type of magnetic resonance imaging (MRI), where magnetic properties of tissues are used to get insight into the imaged body part. In MRI, magnetic fields and magnetic field gradients are applied around the subject making hydrogen atoms in the body of the subject align with the fields. Measurable signals are created by exciting the atoms with radio-frequency pulses, where the signals depend on the type of tissue being imaged and the settings in the MR scanner [13].

There are different settings that can be used to affect how tissues are displayed in MRI and specifically affect how the tissues are weighted. For instance, T1-weighted images normally result in a high signal from fat, making the white matter of the brain bright, and a smaller signal from water, making the cerebrospinal fluid and the gray matter darker. On the other hand, T2-weighting results in images with

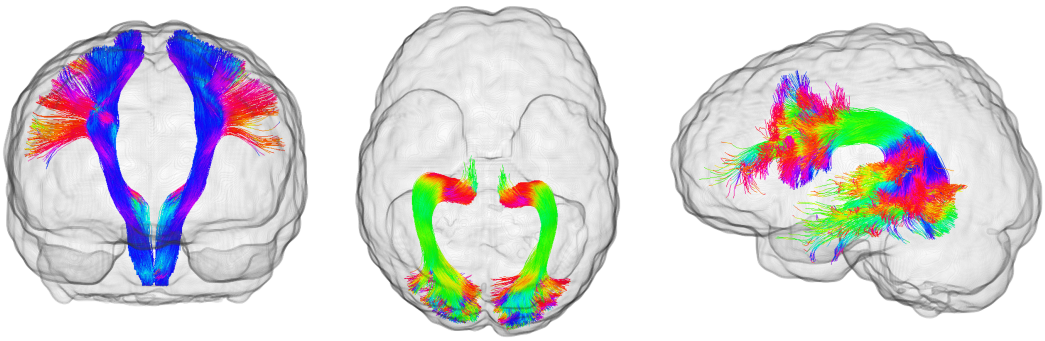

Figure 2.2: Tracts visualized in 3D Slicer[11] using TractSeg[12] on data from the Human Connectome Project. From left: corticospinal tract in anterior view, optical radiation in inferior view, and lateral view of the right arcuate fascicle. Blue indicates that the direction of the tract is superior-inferior, red is for the right-left, and green symbolizes the anterior-posterior direction of the tract.

bright areas where there is a lot of water and dark where there is more fat. Another option is to create contrast based on diffusion, which is done in DWI [13].

DWI is done by applying two extra magnetic field gradients to the MR scheme. The principle can be seen in Figure 2.3. First, a dephasing gradient is applied and after some time a rephasing gradient is applied, which is the opposite of the first gradient. If the hydrogen atoms stay in the same physical location the rephasing gradient will make them return to where they were before the dephasing gradient. However, if there is diffusion in the tissue, the atoms will move to other locations and not receive the opposite of the first dephasing gradient, which leads to signal loss in DWI [14].

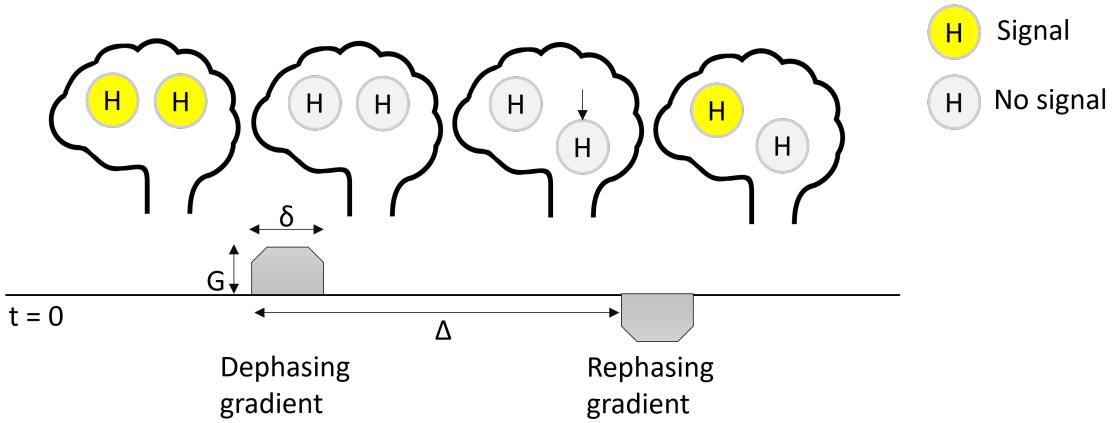

Figure 2.3: Visualization of the idea behind DWI. Two hydrogen atoms are in phase and can send a signal, a dephasing gradient is applied, one hydrogen atom diffuses away and does not receive the rephasing gradient, which leads to signal loss.

The signal loss in DWI depends on the rate of diffusion and properties of the extra

gradient pair. The gyromagnetic ratio of hydrogen γ, the amplitude G and duration δ of the gradient, and the time between the two gradients Δ, are combined to the b-value (s/mm^2) via

$$b = \gamma^2 G^2 \delta^2 (\Delta - \delta/3). \tag{2.1}$$

A higher b-value indicates more diffusion weighting and a b-value of 0 s/mm^2 means no diffusion weighting [15].

Diffusion is the random movement of water, where the water molecules bump into one another and move in any direction where there is no obstacle. Water can diffuse along the tracts of the brain, creating a direction of diffusion. If the diffusion has directionality, it is called anisotropic diffusion, otherwise, it is called isotropic diffusion. Although a DWI image acquired with one set of dephasing and rephasing gradients can give information about if there is diffusion and magnitude, it can not determine the direction. To determine the direction of diffusion and perform tractography (to obtain the tracts of the brain) it is necessary to apply multiple gradients in different directions [14]. The information of the directions is stored in b-vectors, which contain three values for each b-value that correspond to the x, y, and z directions of the applied gradients [16]. Additionally, to motivate the need for multiple diffusion gradients to determine the direction of diffusion, consider that the diffusion gradients are applied in the y-direction and there is diffusion in the x-direction, then there would be no signal loss. On the other hand, if the gradients were in the x-direction, the diffusion in the x-direction would lead to signal loss.

After performing DWI on a subject, the resulting data will be a 4D image, with one 3D image for each gradient direction. Figure 2.4 illustrates how the different dimensions of DWI images are connected to descriptions in this thesis. *DWI slice* is a 2D slice, which will be the type of image that is displayed most often in illustrations. *DWI volume* or *DWI image* is one 3D volume containing all the DWI slices, making up a 3D representation of the brain. Finally, *DWI images* is a broad term describing all the 3D volumes that make up the 4D image, which is the complete set of the DWI data for a subject.

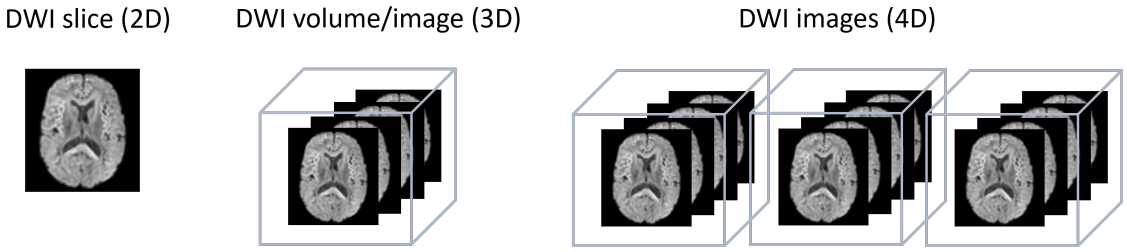

Figure 2.4: The difference in words between dimensions of DWI images.

2.3 Tractography

The process of obtaining nerve tract approximations from DWI images is called tractography [15]. Figure 2.2 displays visualizations (tractograms) of three tracts after

tractography has been performed. There are many methods to perform tractography, ranging from manual to automatic workflows, and utilizing different mathematical concepts. Tractography generally starts with finding the fiber orientation in each voxel (3D pixel), followed by tracking of the fibers and clustering the fibers to form the different tracts [16]. There are different methods for finding the fiber orientation and the ones described in this thesis will be: tensor-based via diffusion tensor imaging, and constrained spherical deconvolution. After finding the fiber orientation and performing either deterministic or probabilistic fiber tracking, it is common to use manual segmentation to perform the clustering to form the different tracts in a clinical setting. Manual segmentation is however time-consuming and relies on the performance of the expert, but it can be done automatically with newly developed technologies [12], as will be done in this thesis.

2.3.1 Diffusion tensor imaging

The most common method to find the fiber orientation of each voxel is to utilize a tensor model, and the subsequent area of study is hence called diffusion tensor imaging (DTI). In DTI, the diffusion in a voxel is represented with an ellipsoid (see Figure 2.5), having one principal axis representing the principal diffusion direction. An ellipsoid can be defined with six parameters; three eigenvectors defining the orientation of three perpendicular axes pointing in the longest ($\mathbf{v_1}$), middle ($\mathbf{v_2}$), and shortest ($\mathbf{v_3}$) direction of the ellipsoid, and three eigenvalues (λ_1, λ_2, λ_3) defining the length of the three axes.

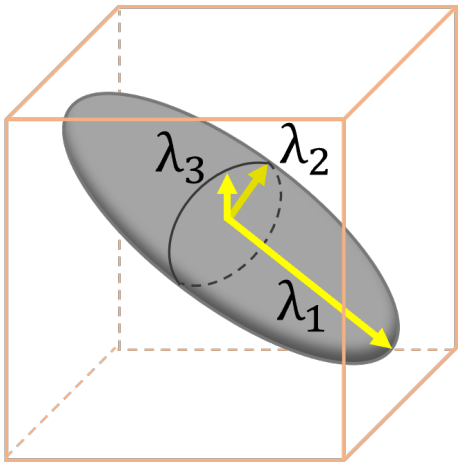

Figure 2.5: Ellipsoid in a voxel with three eigenvectors and their corresponding eigenvalue marked in the figure.

To measure diffusion and compare it between different tracts or subjects, there are a few different metrics that can be calculated based on the tensor model in DTI. The eigenvalues of the diffusion tensor can be combined to measures of axial diffusivity (AD), mean diffusivity (MD), and radial diffusivity (RD). AD is equal to λ_1, while MD is the average of all eigenvalues, and RD is the average of λ_2 and λ_3. Yet, the

most common metric is fractional anisotropy (FA)

$$FA = \frac{1}{\sqrt{2}} \frac{\sqrt{(\lambda_1 - \lambda_2)^2 + (\lambda_2 - \lambda_3)^2 + (\lambda_3 - \lambda_1)^2}}{{\lambda_1}^2 + {\lambda_2}^2 + {\lambda_3}^2}, \tag{2.2}$$

which estimates how much the ellipsoid differs from a perfect sphere. An FA value of zero indicates that the diffusion is estimated with a sphere, and a higher FA indicates that the diffusion in a voxel is more anisotropic and has more directionality [14]. Attempts have been made to connect FA to microstructural properties of the white matter, and is commonly interpreted as a measure of white matter integrity [16]. Although, FA can depend on other factors than the integrity of the white matter, e.g., axon density and axon diameter [17].

The power of DTI lies in the low number of DWI images per patient required to find the fiber orientation in a voxel and the resulting short image acquisition time. One limitation is the assumption that one voxel only contains one fiber, which can be false in voxels where fibers cross [16].

2.3.2 Constrained spherical deconvolution

An alternative to DTI is to obtain the fiber orientation using constrained spherical deconvolution (CSD), which has been proven to handle fiber crossings better than DTI [16]. CSD estimates the fiber orientation distribution (FOD) of a voxel by assuming that the signal in each voxel is the spherical convolution between a response function and the FOD, where the response function is the diffusion-weighted signal of a voxel with only one fiber along the z-axis. Spherical convolution utilizes spherical harmonics, Fourier transforms of spherical signals, as basis functions for the signal. Constrained spherical deconvolution is done to obtain the FOD, where the constraint is non-negativity on the FOD to reduce noise [18].

Figure 2.6 illustrates the difference between the tensor model and FOD in two different cases. If there is just one direction of diffusion, i.e., one direction of the fibers in a voxel, both the tensor model and FOD can satisfactorily characterize the diffusion. On the other hand, if there is a crossing of fibers, the tensor will not be able to differentiate the fibers, while the FOD can.

2.4 DWI pre-processing

DWI images with a nonzero b-value typically have lower resolution than T1- or T2-weighted images, which can be because of a fast acquisition scheme or if a lower magnetic field strength has been used. Furthermore, DWI images are sensitive to noise and can have a low signal-to-noise ratio [19]. There are also different artifacts and distortions that can affect DWI images, which can be corrected to improve the analysis of the images. The pre-processing pipeline has to be adapted to the data at hand, depending on each situation and the MR machine used. The most common

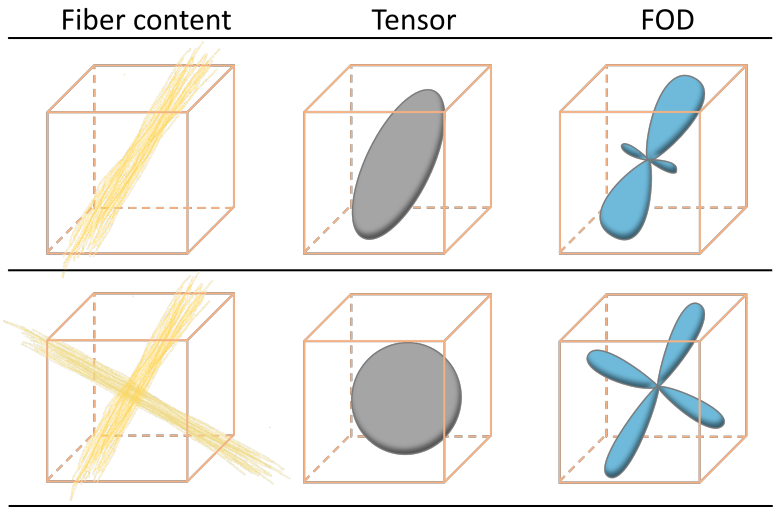

Figure 2.6: Two different fiber contents in voxels are modeled differently with a tensor and an FOD.

artifacts for DWI and their state-of-the-art correction methods which have been considered for this thesis can be found in [20], and below is a brief description of the artifacts relevant to this thesis.

2.4.1 Noise

Noise in DWI images is a random fluctuation that typically comes from the movement of electrolytes within the patient or from the receiver coil [21]. The noise makes the images look blurry and reduces the possibility of distinguishing anatomical features. Apart from hindering visual inspection, the noise can be amplified when deriving quantitative metrics from the DWI images and affect their values [20].

2.4.2 Gibbs ringing artifacts

MR images are acquired in frequency domain with the frequency content ranging from low to high frequencies, but it is impossible to include all the high frequencies when reconstructing the images, therefore, it is necessary to truncate the frequencies. If this is done too abrupt it can lead to an artifact called Gibbs ringing, which will result in an image with oscillating features [20] with multiple fine lines close to high-contrast interfaces. For DWI, Gibbs ringing could be a less significant problem because of the low resolution, and hence the distortions can not be seen [16]. It is however quite common to correct for them if deemed necessary [22]–[24]. Moreover, the ringing artifacts could affect metric values that are calculated from multiple DWI images, such as FA values, since the artifact could be cumulative and lead to worse approximations [20].

2.4.3 Susceptibility-induced distortion

When certain acquisition protocols are used to acquire DWI images and the magnetic fields contain inhomogeneities, susceptibility-induced distortion can occur [14]. Susceptibility-induced distortions cause geometrical distortions and signal dropout and mostly affect areas with tissues of different susceptibility [25]. An example of how the distortions can look is displayed in Figure 2.7, where an unprocessed DWI slice with distortions anterior to the auditory canals is visualized in 2.7a, while 2.7b displays the same slice after correction.

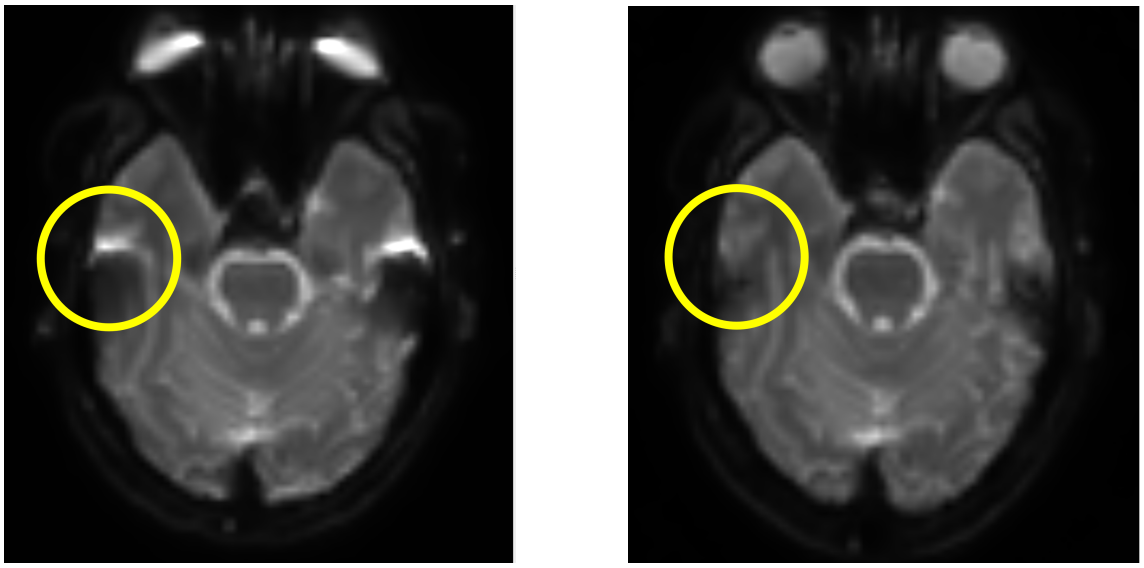

(a) Unprocessed DWI slice

(b) Processed DWI slice

Figure 2.7: DWI $b = 0$ slices (i.e., no diffusion weighting), before and after correction for susceptibility-induced distortion. The area of interest is encircled.

2.4.4 Eddy currents and motion artifacts

While susceptibility-induced distortions affect all DWI volumes of a patient in the same way, eddy currents, and motion artifacts can result in different shear distortions in all volumes. The eddy currents can come from the magnets, coils, imperfections in the diffusion gradients, or from some gradients lingering too long in the tissue [14]. Consequently, the lingering gradients can combine with the spatial encoding gradients to alter the read-out signal, which leads to geometrical distortions [20]. Motion artifacts also lead to geometrical distortions, but come from when the patient moves in the MR scanner.

2.4.5 Bias field

If there is intensity variation within a tissue in an MR image, it is possible that there is a distortion called bias field. The bias field can come from inhomogeneity in the magnetic fields or the RF-coils, but also from patient movement [26]. If analysis of DWI should be done based on the assumption that one tissue has the same intensity, bias fields can cause issues [27]. Yet, bias field correction is not as common to do as

the steps described above [20], but it is adopted when deemed needed, for example in [22], [23], [28], and [29].

2.4.6 Registration

After distortion correction, the DWI images are typically registered to a standard atlas, aligning the images to the same coordinate system. The most common atlas is the Montreal Neurological Institute (MNI) space, which is made from a co-registration of 152 brains. Registration is done in order to be able to compare different patients' brains [30]. Either the image is rigidly aligned to MNI, meaning it is aligned to the coordinate axes of MNI, or the image can be registered to MNI with a specified size and shape of the brain. These two types of registrations can be achieved by applying linear transformations and to align the coordinate axes of the image to MNI. A rigid transformation with six parameters that can rotate or translationally transform the image. To register the image to MNI with size and shape too, an affine transformation with 12 parameters is applied, which can enable rotation, translation, and stretching of the image [31].

2.5 Quantitative tract analysis

The metrics used for quantitative tract analysis can be divided into two types, microstructural metrics and metrics that come from morphological features of the computed tracts. Microstructural metrics are related to the microstructure of the tracts, for example, FA and other metrics. Examples of morphological features are the size of the tract or the number of streamlines in each tract [32].

When analyzing tracts from glioma patients, the most common approach is to perform tractography by using DTI and computing various tensor-based metrics, such as FA, AD, MD, and RD for analysis. Even though other methods than DTI are used for tractography, tensor-based metrics are often used for analysis [33]–[35]. There are other metrics that can be derived, for instance from the FOD, one being the amplitude of a peak of the FOD, termed peak length. Furthermore, the metrics can either be compared voxel by voxel, averaged for each tract, or it is possible to compute metrics along the tracts. It has been seen that computing metrics along tracts, rather than just one average, has benefits for analysis [36]. For example, the FA-values of a tract can vary a lot along the tract, and if a person has an alteration in the tract that makes FA higher in one area and also lower in another, an average FA-value would not show any difference.

3

Methods

The Methods include a description of the data sets used in the project and their properties, followed by a presentation of the workflow to perform tractography on them, with an emphasis on pre-processing the glioma patients' images. Furthermore, a section is included with the selected quantitative analysis of the tractography results is explained.

3.1 Glioma imaging data

MR images from 16 glioma patients were included in the project, collected at Sahlgrenska University Hospital. Anonymized T1-weighted images in MNI and DWI images were made available for this project. T1 images were obtained for anatomical visualization and visual inspection of resulting DWI tracts and their location, T1 image processing or analysis was not part of this thesis project. The obtained DWI images were of the following properties: collected by a single-shell (a single b-value) acquisition protocol with 64 gradient directions, one reverse phase-encoding $b = 0$ image and with a voxel size of 2.33 mm^3.

The workflow to process the glioma patients' DWI data to perform tractography is illustrated in Figure 3.1. Firstly, a series of pre-processing steps were performed, and secondly, the open-source white matter segmentation tool TractSeg[12] was applied. The pre-processing steps are described below with functions and parameters and a brief description of the algorithm each function implements, followed by an explanation of the TractSeg methodology and a motivation for the choice of TractSeg to perform tractography.

3.1.1 Pre-processing

Pre-processing of the glioma patients' images was done with functions from the software packages: MRtrix3[37], FSL[38]–[40], and DIPY[41]. Firstly, denoising was done using MRtrix3 function `dwidenoise`[37], [42]–[44]. The function estimates noise based on the redundancy of data that comes from the multiple diffusion volumes. By using random matrix theory it is possible to fit a distribution (Marchenko-Pastur distribution) to the eigenspectrum (set of all eigenvalues) of the signal and

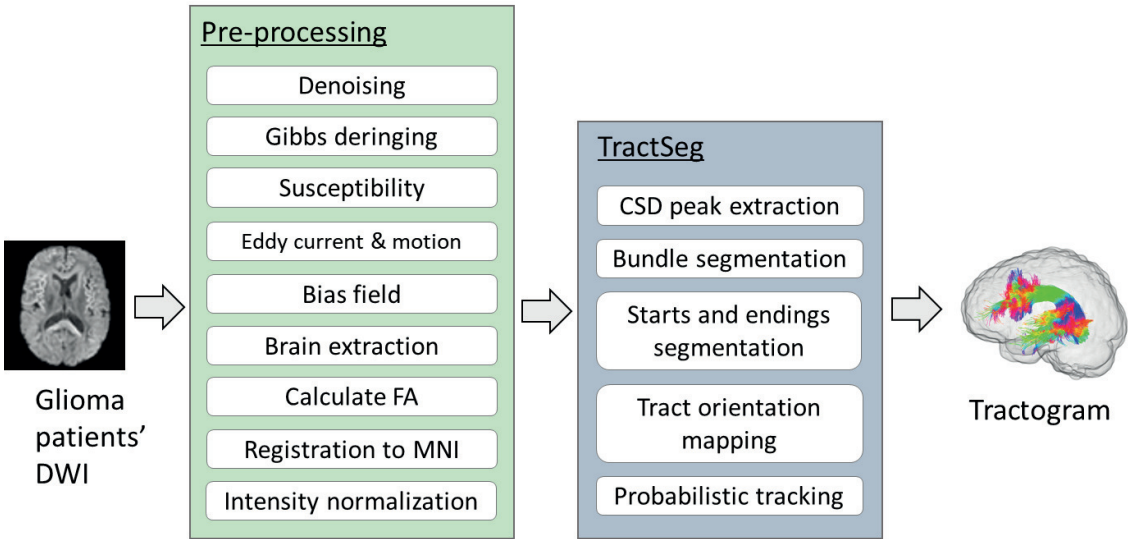

Figure 3.1: Flow chart for the automatic processing workflow of the glioma patients' DWI images.

estimate the noise. This step must be done first before any other steps. The residuals (noisy image subtract denoised image) were visually inspected to make sure no anatomy could be seen, which would indicate that the denoising was not successful.

After denoising followed the removal of Gibbs ringing artifacts with `mrdegibbs`[37], [45]. The function applies a method based on local subvoxel-shifts to reinterpolate the image and overcome the truncation that was done by the low-pass filter [45].

Susceptibility-induced distortion correction, eddy current, and motion correction using a $b = 0$ image with reversed phase encoding are all included in `dwifslpreproc`[25], [37], [39], [46]. The settings used were `-rpe_pair`, which specifies that a pair of images of opposing phase encoding are included, and the pair is specified with `-se_epi`. Additionally, to make sure the pair of images are registered to each other, the option `-align_seepi` was included. With these described settings `dwifslpreproc` maximizes the similarity between the two $b = 0$ images of opposite phase encoding and by that estimates the changes to the DWI images needed to correct for susceptibility-induced distortions [25]. On top of that, the function will correct for eddy currents and motion artifacts by predicting how the images should look by modeling the diffusion signal as a Gaussian Process and then iteratively updating the corrections needed from the error between the predicted images and the observed [46].

Bias field correction was performed using the N4 algorithm from ANTs (Advanced Normalization Tools) in the MRtrix3 function `dwibiascorrect ants`[37], [47]. The N4 algorithm performs normalization of the DWI volumes using algorithms that maximize high frequencies in the distribution of intensities in the volumes [47]. No extra parameters were needed for the function.

After correcting the DWI images, brain extraction was performed to ensure only

brain areas are included in the subsequent processing. FSL's tool `BET`[48] was used with a fractional intensity threshold of 0.5 and a vertical gradient of 0 to generate brain masks.

FSL's tool `fslreorient2std` was applied before the registration to correct for axes of the DWI images (right-left, anterior-posterior, superior-inferior) not matching with MNI standard space, in which case the images are reoriented. The registration was then done by first computing an FA image based on all DWI volumes for a patient and estimating the transformation needed to register the FA image to the corresponding patient's T1-weighted image in MNI-space. The affine transformation was estimated using the `flirt`[49]–[51] function in FSL, with 12 degrees of freedom and mutualinfo as cost function. To register all the DWI volumes to MNI, the transformation estimated by `flirt` was applied with the options: applyisoxfm, 12 degrees of freedom, and spline interpolation. The registration results were controlled manually by inspection of the spatial agreement between the registered image and an MNI-space brain mask.

Intensity normalization was done with `dwinormalise group`[37], which required all subjects to be normalized at the same time, and therefore, both the glioma patients' and the healthy subjects' images were normalized at the same time. The function used an algorithm based on the median $b = 0$ white matter value to normalize the intensities.

3.1.2 TractSeg

TractSeg[12] is an open-source white matter segmentation tool for tractography by performing fiber tracking and sorting the fibers into 72 different tracts, see Table A.1 in Appendix A. The main components of the tool are three 2D encoder-decoder artificial neural networks that are trained via supervised learning on Human Connectome Project (HCP) data. The inputs to each network are FOD peaks. Here they were obtained by performing CSD, which was done by using a modified version of TractSeg's source code, to enable the comparison between subjects by applying the same response function to all subjects. The response function was chosen to be the average of all subjects' response function obtained using `dwi2response tournier`[37], [52] from MRtrix3, followed by `responsemean`[37]. `dwi2fod csd`[18], [37], [53] was used to compute FODs by applying CSD, and `sh2peaks`[37], [54] to compute the peaks of the three principal diffusion directions from each FOD.

TractSeg's three encoder-decoder networks result in tract segmentations, tract orientation maps (TOM), and start and end region segmentations, where TOMs are orientation maps for each tract with one FOD peak per voxel. Creating the final tractograms is also done in TractSeg, using a probabilistic algorithm that requires the peaks, the tract segmentations, the ending segmentations, and the TOMs. The obtained tracts consist of a maximum of 2000 streamlines that goes from the start to the end regions of the segmented tracts [9].

The choice of TractSeg is motivated based on its performance compared to other segmentation tools. When comparing TractSeg to a DTI-based tractography method it was seen that TractSeg showed potential in being more sensitive to microstructural changes, and also being able to handle lower b-values and DWI volumes than the DTI method [22]. Furthermore, comparisons between TractSeg and manual segmentation indicated that TractSeg computes segmentations with more consistency than the manual method [55], [56]. There are other automatic tract segmentation tools, e.g., TRACULA[57], [58] or RecoBundles[59], but TractSeg has been seen to compute tracts with better accuracy than them, and also for images with reduced quality [12].

3.2 Healthy subjects imaging data

The data for the normative population in this project was sourced from the Human Connectome Project (HCP)[60]–[64] Young Adult database, which consists of individuals who are considered to be in a healthy state. Of the over 1100 subjects available, 42 persons were included to represent a healthy population, and those persons are a subset of the data that TractSeg was trained on, see description above. Computational resources limited the inclusion of more healthy subjects. The HCP images were acquired using a multishell (multiple different b-values) acquisition protocol with 190 gradient directions with b-values between 5 and 3010 mm/s^2, and a voxel size of 1.25 mm^3. Figure 3.2 displays the flow chart for performing tractography on the healthy subjects' images, consisting of pre-processing steps, followed by TractSeg, applied according to 3.1.2.

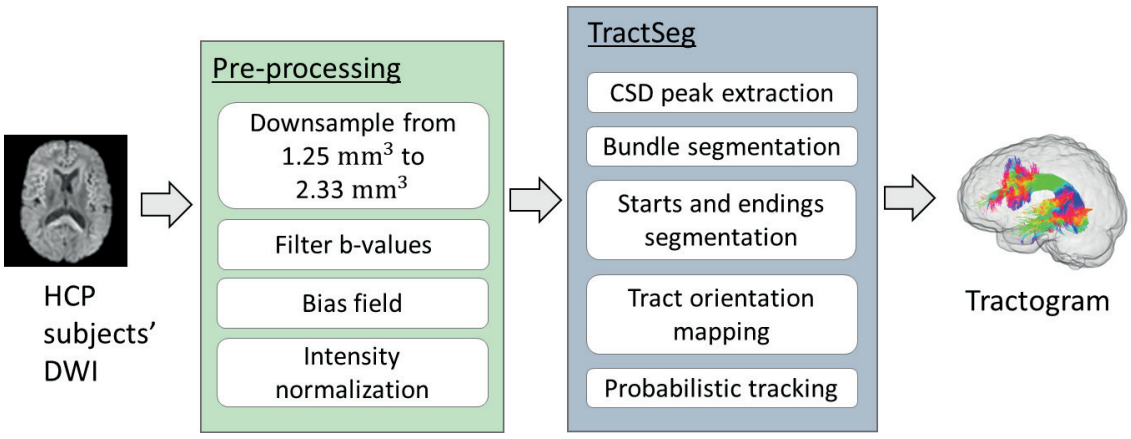

Figure 3.2: Flow chart for the tractography of healthy subjects' DWI images from HCP.

The healhty subjects' images were already pre-processed using a minimal processing pipeline [60] when downloaded from humanconnectome.org, including intensity normalization across runs, correction of eddy currents, motion artifacts, and gradient-nonlinearities, along with registration to the corresponding T1-weighted image and brain mask estimation. However, to enable the comparison between the glioma patients' properties and the healthy subjects', downsampling to a voxel size of 2.33

mm^3 was done using the function `mrgrid` from MRtrix3 with the option `regrid`, and only b-values of 5 or between 995 and 1005 mm/s^2 and their corresponding DWI volumes were included. Furthermore, bias field correction was done using `dwibiascorrect ants`, as described above, and intensity normalization was done using `dwinormalise group`[37] together with the glioma patients.

3.3 Quantitative tract analysis

The quantitative analysis of the obtained tracts was done using TractSeg's Tractometry module, which is based on [65]. For both healthy and glioma patients, metrics were evaluated along the profiles of 50 of the 72 tracts, where the 50 tracts were selected based on the default settings for Tractometry. The metrics included in this analysis were FA and the peak length of the FOD. Metric maps of FA were calculated using the tensor model from DIPY, and the peak lengths of the FODs were obtained via the norm of the TOM amplitudes. Computing the tract profiles is illustrated in Figure 3.3. All streamlines in a tract were divided into 100 segments, and by mapping the coordinates of the streamlines to the metric maps, the segments were assigned values of the metrics. For each tract, one center streamline with 100 segments was determined and each segment of the other streamlines got assigned to the closest center streamline segment. Thereafter, the metric values of all segments that belong to a center streamline segment were averaged to produce 100 values along the center streamline, representing the tract profile.

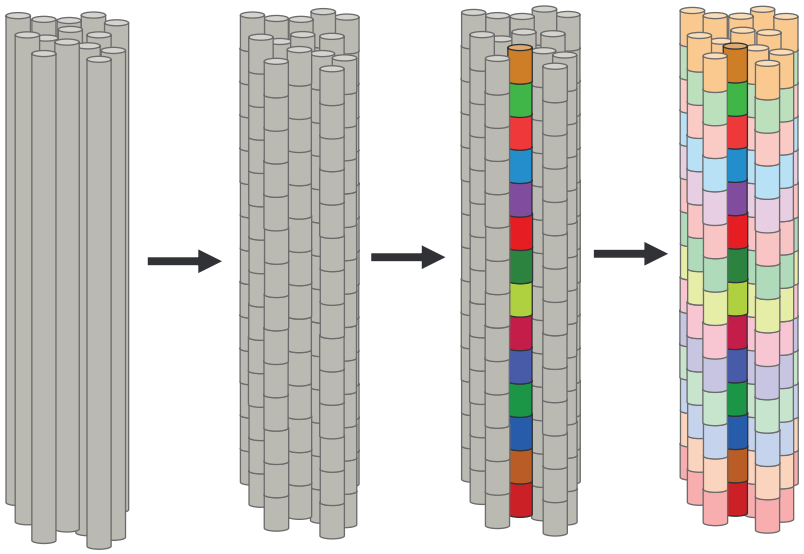

Figure 3.3: Computing tract profiles according to TractSeg's Tractometry module. From the left, streamlines of a tract are visualized, streamlines are divided into segments, a center streamline is determined, and the segments of all streamlines are assigned to the closest center streamline segment.

The number of significant points along the tract profiles was counted for all patients and if a tract had more than 20% significant values of the 100 values the tract in question got a vote, leading to all glioma patients voting on the most affected

tracts. This process was followed for all patients to measure the most affected tracts. The choice of setting the level at 20% was based on empirical considerations to avoid excessive or insufficient discrimination in the classification of affected tracts. However, there is room for improvement in the classification criteria.

The significance was calculated by statistical comparison between corresponding tract values of all used healthy subjects and the glioma patient using the Crawford-Howell test, which has shown a potential to be appropriate to determine if one sample belongs to a certain distribution [66], meaning if one point in a tract profile of a glioma patient has a metric value differing from the corresponding value of the healthy population. The test statistic for the Crawford-Howell test was defined as

$$t = \frac{|x_{glioma} - \bar{x}_{healthy}|}{s\sqrt{(n+1)/n}} \tag{3.1}$$

where x_{glioma} is one glioma patient's metric value and $\bar{x}_{healthy}$ is the average of the corresponding value for all the healthy subjects, s and n are the standard deviation and the number of the healthy subjects, which was 42 in this thesis. A 99% two-sided t-test was done and p-values were obtained using `Scipy.stats.t.cdf` via

$$p = 2(1 - \texttt{Scipy.stats.t.cdf}(t, n-1)), \tag{3.2}$$

where `Scipy.stats.t.cdf` extracts the probability from the cumulative distribution function of the t-test. If the p-value is lower than 0.01 it is possible to reject the null hypothesis that the glioma patient's measure comes from the same distribution as the healthy subjects and the value is classified as significant.

A further quantitative tract analysis was done by investigating the number of streamlines TractSeg produced for each tract and counting the number of glioma patients with less than 2000 streamlines for each tract.

4

Results

The Results include examples of the effects of the pre-processing for one representative glioma patient in terms of both before and after registration. Furthermore, examples of the resulting tracts for different patients from TractSeg are displayed, and the results of the comparison between the glioma patients and the healthy subjects are presented.

4.1 Pre-processing of glioma patients' DWI

The pre-processing outline described under Methods was applied to the 16 glioma patients. Visual inspection of the residuals from denoising concluded that none of the patients' residuals had any outlines of anatomy. An example of the results after performing denoising, deringing, susceptibility-induced distortion correction, eddy current and motion correction, and bias field correction can be seen in Figure 4.1. Figure 4.1a displays one sagittal slice of the brain of an unprocessed DWI volume and 4.1b displays the same slice after the pre-processing steps. Note that the intensities are altered and by looking at the most anterior point of the brain in both images, it is possible to see the effect of the geometrical corrections.

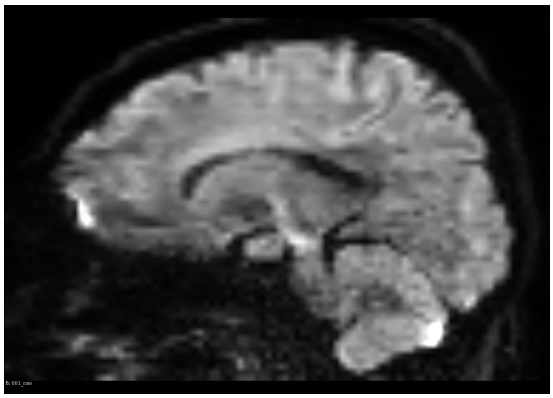

(a) Unprocessed DWI

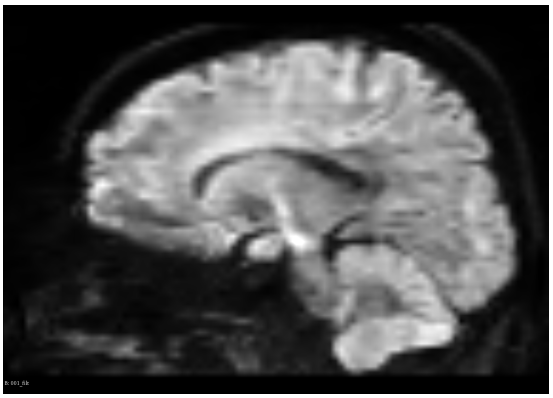

(b) Processed DWI

Figure 4.1: Effect of performing denoising, deringing, susceptibility-induced correction, eddy current and motion correction, and bias field correction on a sagittal DWI slice.

Registration to MNI is the last step in the pre-processing workflow before intensity normalization and to illustrate the results of registration, Figure 4.2 displays axial, coronal, and sagittal slices for the $b = 0$ DWI volume of a glioma patient, where the slices in the top row are before registration and in the bottom row are the slices after registration. The outlines of an MNI mask are overlayed on the DWI slices and are visualized in green, and they differ a lot between the top and bottom row due to the differences in coordinate systems before and after registration. Moreover, the lack of alignment between the slices in the top row and the mask indicates the transformations needed to register the DWI to MNI. The bottom row is aligned with the mask and the registration was considered successful, which was the case for all 16 patients, and no further modifications were needed.

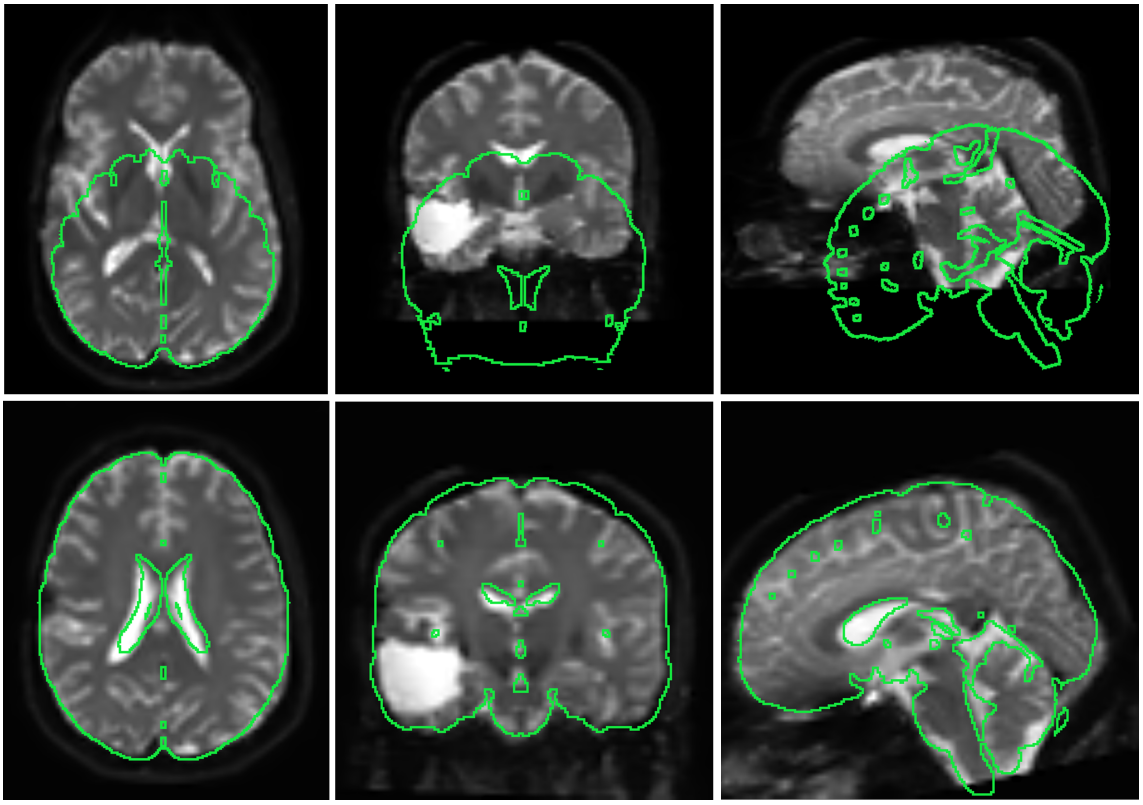

Figure 4.2: Effect of registration. The top row contains slices from a b=0 DWI volume before registration and the bottom row shows slices with the same index after registration. The green outlines indicate the wanted MNI anatomy.

4.2 TractSeg on glioma patients' DWI

TractSeg successfully computed 100% of the expected 72 tracts for all healthy subjects, and for the glioma patients, 99.0% were computed (11 failed of 72x16 expected). A tract was considered failed if the number of streamlines was zero. The failed tracts originated or ended in regions where the tumors have been resected, i.e., no white or gray matter was present in those areas.

Figure 4.3 displays example output from TractSeg for one representative healthy subject in the upper part of the figure and for two glioma patients in the lower part, where the superior longitudinal fascicle (SLF) III, the inferior fronto-occipital fascicle (IFOF), and the uncinate fascicle (UF) are visualized. Compared to the corresponding tracts in the healthy subject, the anterior part of the left SLF III is more superior and curved around the surgical site, the right IFOF is narrower, and the right UF is displaced. Only the IFOF of patient 2 lacks streamlines, where 1610 of 2000 were obtained.

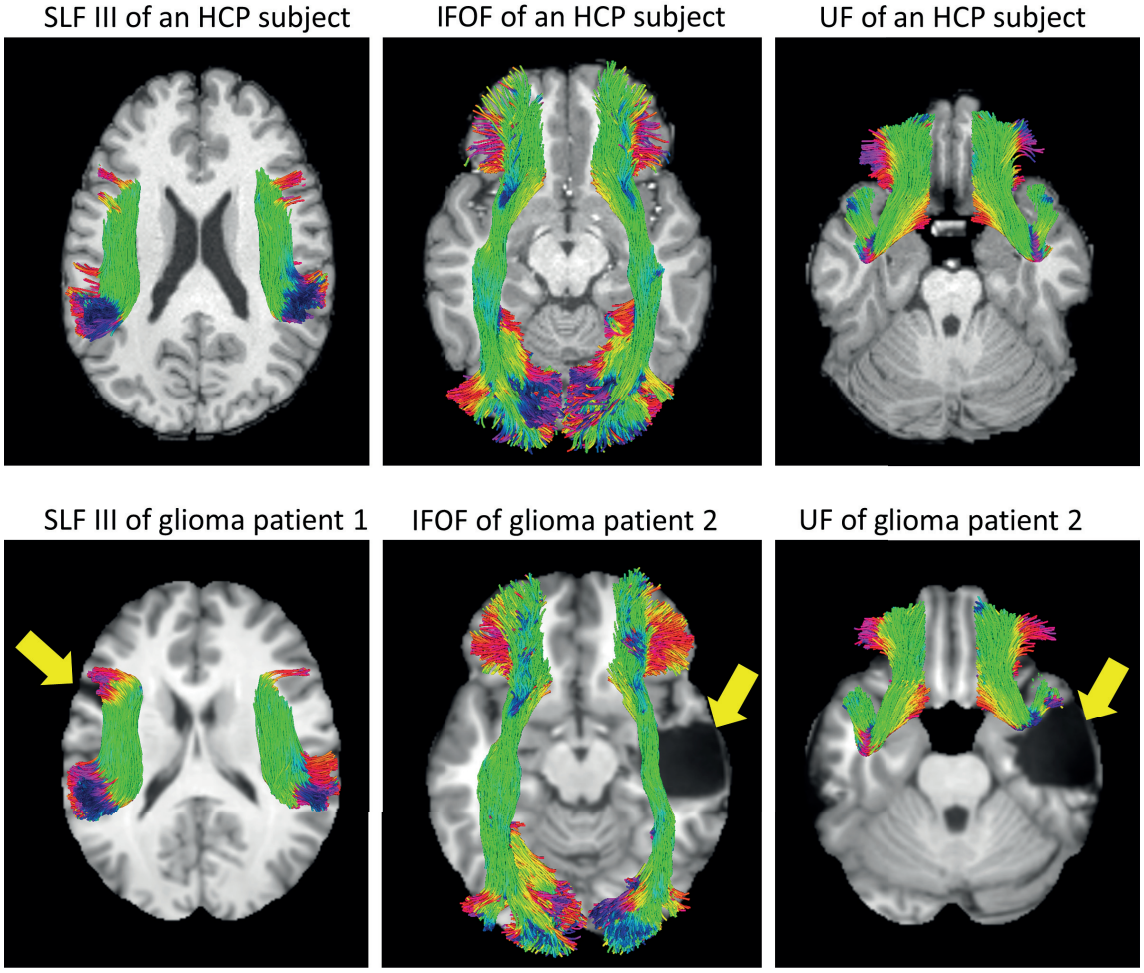

Figure 4.3: Upper part: superior view of slices and tracts of a healthy subject (termed HCP in the figure), lower part: superior view of slices and tracts of two glioma patients where arrows indicate where the tumors have been resected. From left: the superior longitudinal fascicle (SLF) III, the inferior fronto-occipital fascicle (IFOF), and the uncinate fascicle (UF).

4.3 Quantitative measures and analysis

The results of the comparison between glioma patients and healthy subjects are first presented based on individual FA comparison, where tracts of two glioma patients are included to display examples of the FA changes for all glioma patients' tracts. Next, the most affected tracts are presented based on both FA and peak length comparisons. Finally, a tract group comparison is presented where the glioma cohort is compared to all healthy subjects for the most affected tracts.

4.3.1 FA changes for glioma patients

Individual FA comparisons between all 16 glioma patients' tracts to the corresponding tracts of all healthy subjects were done and a selection of the comparisons is included here as three cases. In the first case in Figure 4.4, the right UF of patient 2 had significantly lower FA than the healthy subjects at parts of the tract profile, with the tract having the expected number of streamlines. Similar features apply to the second case in Figure 4.5, the left AF of patient 3, with lower FA than the corresponding tract in the healthy subjects and a full number of streamlines, but that tract was interrupted due to the tumor. The third case in Figure 4.6 shows the interrupted tract CC 3 for patient 3, where only a fraction of the streamlines were computed (130 of 2000 were computed), and the FA tract profile appears to be shifted to the right.

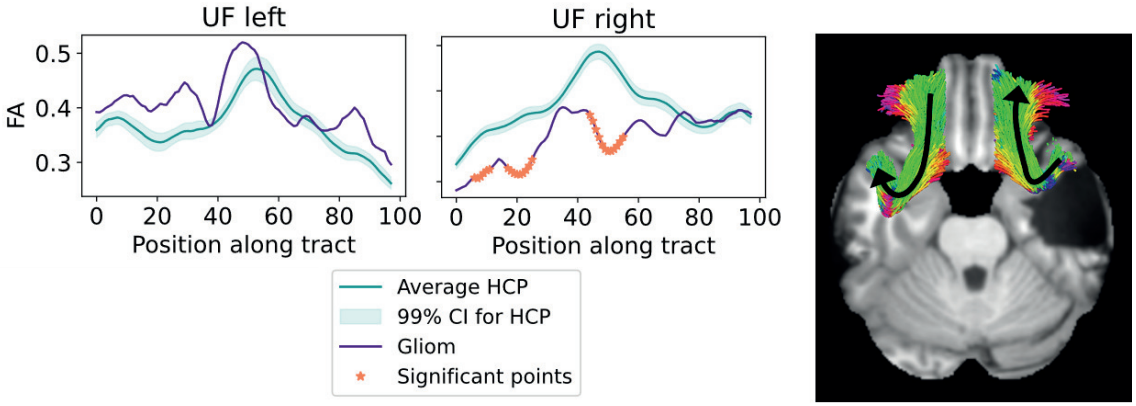

Figure 4.4: FA comparison between healthy subjects (termed HCP in the figure) and glioma patient 2 for the uncinate fascicle (UF). A 99% confidence interval is included for healthy subjects and the significant points based on the Crawford-Howell test at 0.01 level are marked. To the right in the figure is a depiction of the left and right UF on a T1-weighted slice in superior view for the patient with the tract profile directions marked with arrows.

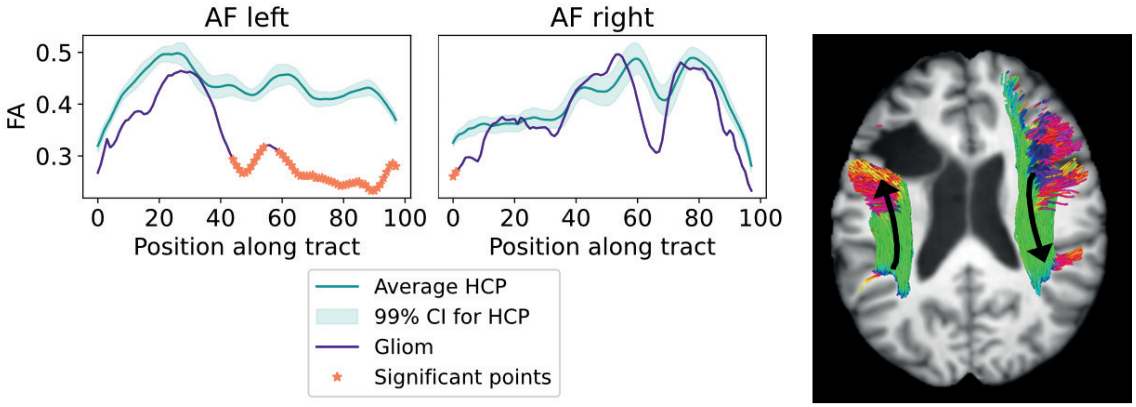

Figure 4.5: FA comparison between healthy subjects (termed HCP in the figure) and glioma patient 3 for the arcuate fascicle (AF). A 99% confidence interval is included for the healthy subjects and the significant points based on the Crawford-Howell test at 0.01 level are marked. To the right in the figure is a depiction of the left and right AF on a T1-weighted slice in superior view for the patient with the tract profile directions marked with arrows.

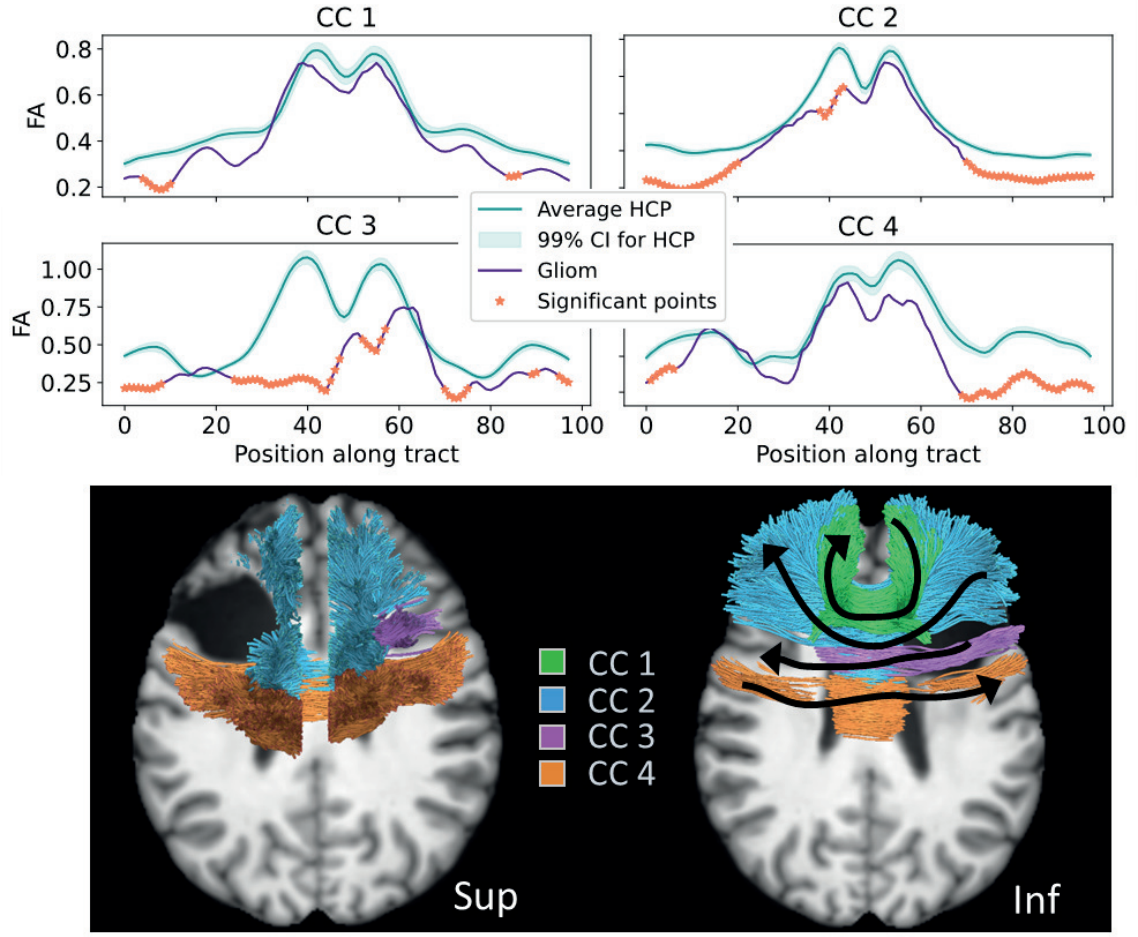

Figure 4.6: FA comparison between healthy subjects (termed HCP in the figure) and glioma patient 3 for corpus callosum (CC) 1-4. A 99% confidence interval is included for the healthy subjects and the significant points based on the Crawford-Howell test at 0.01 level are marked. The bottom left part of the figure contains a depiction of the patient's CC 2-4 on a T1-weighted slice in the superior (Sup) view, and since CC 1 can not be seen, the right part is displaying the inferior (Inf) view. The tract profile directions are marked with arrows in the inferior view.

A tract of a glioma patient was considered affected if more than 20% points were significant according to the Crawford-Howell test, see the orange markings in Figure 4.4, 4.5 and 4.6. Note that the whole tract is colored if it is considered affected, and not just the parts that contained the significant points. The full tractograms with affected tracts for glioma patients 3 and 4 can be seen in Figure 4.7. Glioma patient 4 had a larger surgical site compared to glioma patient 3.

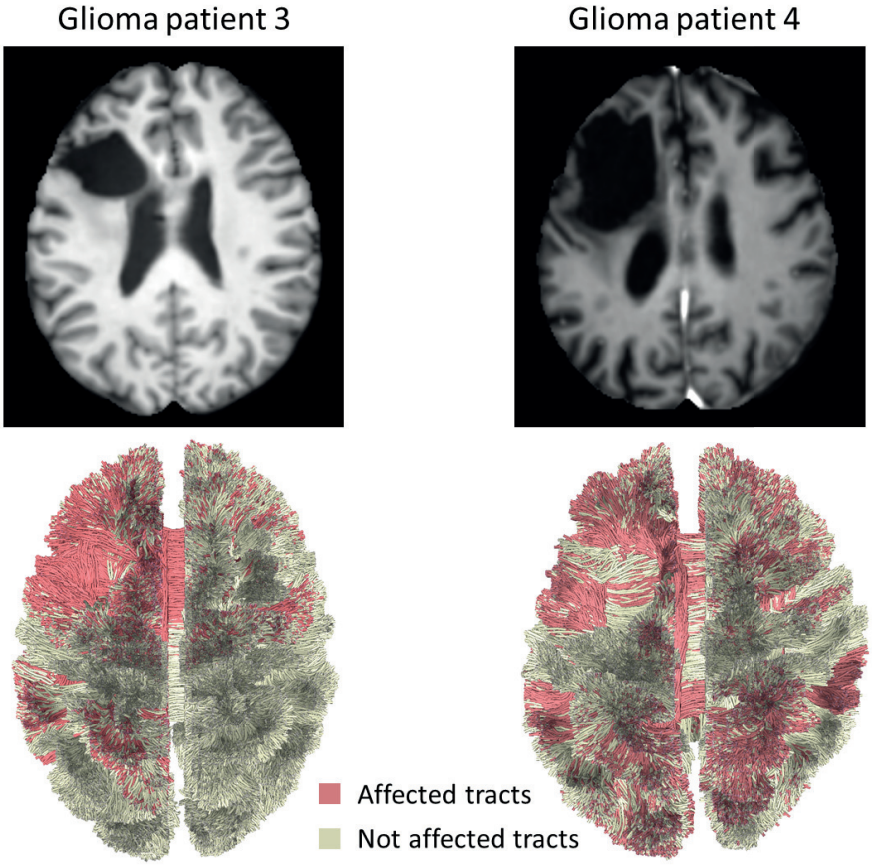

Figure 4.7: T1-weigthed images and full tractograms for glioma patients 3 and 4. The tracts are determined to be affected if more than 20% of the FA points along the tract profiles are significant.

4.3.2 Most affected tracts

The quantitative comparison between glioma patients and healthy subjects resulted in Table B.1 in Appendix B, of which the most affected tracts based on FA and peak length comparison are presented in Table 4.1. The values in the table represent the number of glioma patients with more than 20% significant points. Table 4.1 includes tracts for the FA and peak length comparisons if the number of patients is greater than seven and eight, respectively. The most affected tracts according to both the FA and the peak length comparison were the anterior thalamic radiation (ATR), corpus callosum (CC) part 1-3, and striato-fronto-orbital fascicle (ST FO). The FA comparison also resulted in the CC 4, cingulum (CG), thalamo-occipital tract

(T OCC), and the superior longitudinal fascicle (SLF) III, while the peak length comparison distinguished the thalamo-premotor tract (T PREM), SLF II, thalamo-parietal tract (T PAR), striato-premotor tract (ST PREM), and the parieto-occipital pontine tract (POPT).

Table 4.1: Tracts and their corresponding number of glioma patients with more than 20% significant points for both FA and peak length comparison. Including the anterior thalamic radiation (ATR), corpus callosum (CC 1-4), cingulum (CG), parieto-occipital pontine tract (POPT), superior longitudinal fascicle (SLF) II and III, striato-fronto-orbital tract (ST FO), striato-premotor tract (ST PREM), thalamo-occipital tract (T OCC), thalamo-premotor tract (T PREM), and the thalamo-parietal tract (T PAR). Note that the CC is bilateral and only one value is displayed for each part.

Tract	FA: left | right	Peak length: left | right
ATR	10 | 9	16 | 14
CC 1	7	9
CC 2	12	14
CC 3	11	10
CC 4	7	7
CG	7 | 4	4 | 5
POPT	0 | 2	8 | 4
SLF II	3 | 5	3 | 8
SLF III	7 | 5	2 | 4
ST FO	9 | 5	12 | 8
ST PREM	4 | 5	8 | 7
T OCC	7 | 2	6 | 1
T PREM	5 | 5	14 | 10
T PAR	4 | 6	10 | 4

4.3.3 Tract group comparison

Group comparisons between all glioma patients and the healthy subjects for a selection of the most affected tracts, based on the FA comparison in Table 4.1, are visualized in Figure 4.8. The included tracts are the anterior thalamic radiation (ATR), corpus callosum (CC) 1-4, cingulum (CG), and striato-fronto-orbital tract (ST FO). Figure 4.9 presents peak length tract group comparisons for some of the most affected tracts based on the peak length comparison, including the ATR, CC 1-4, ST FO, and the thalamo-premotor tract (T PREM).

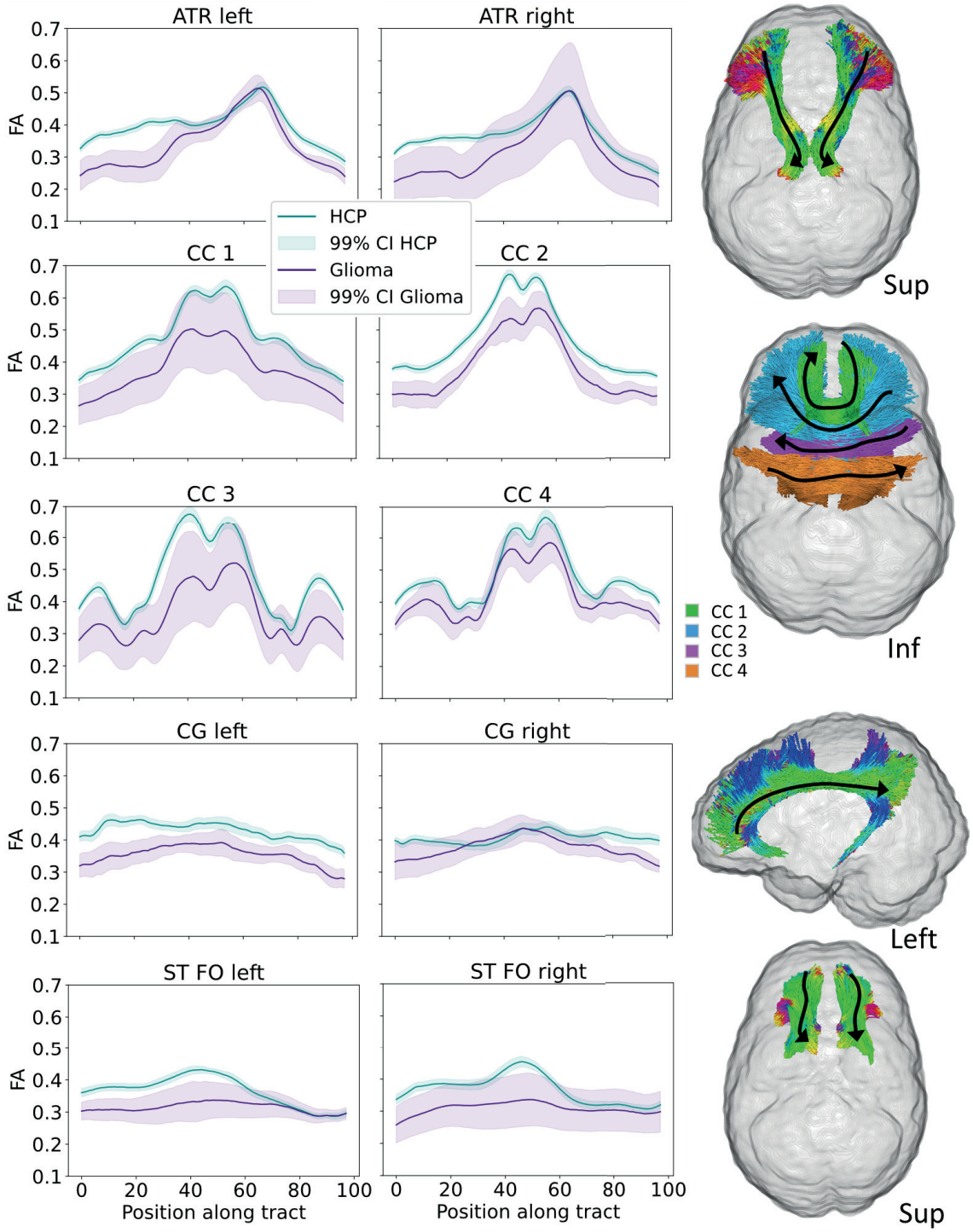

Figure 4.8: FA comparison between healthy subjects and glioma patients along the tract profiles of the included tracts, anterior thalamic radiation (ATR), corpus callosum (CC), cingulum (CG), and striato-fronto-orbital tract (ST FO). 99% confidence intervals are displayed for both healthy subjects (termed HCP in the figure) and glioma patients. Visualizations of the tracts are included to the right of the graphs with the tract profile directions drawn, where the views from the top to down are: superior (Sup), inferior (Inf), left, and superior.

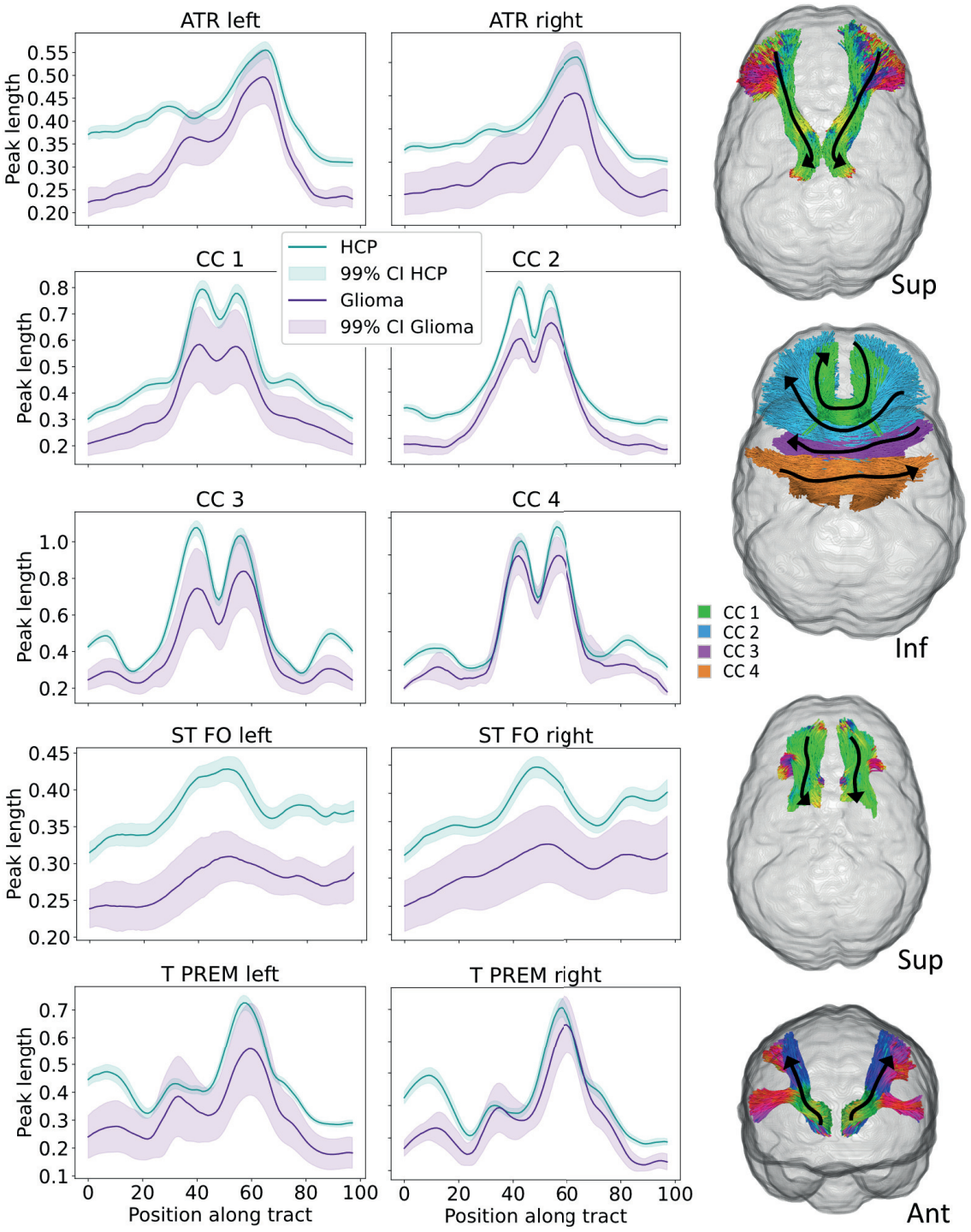

Figure 4.9: Peak length comparison between healthy subjects and glioma patients along the tract profiles of the included tracts, anterior thalamic radiation (ATR), corpus callosum (CC), striato-fronto-orbital tract (ST FO), and thalamo-premotor tract (T PREM). 99% confidence intervals are displayed for both healthy subjects (termed HCP in the figure) and glioma patients. Visualizations of the tracts are included to the right of the graphs with the tract profile directions drawn, where the views from the top to down are: superior (Sup), inferior (Inf), superior, and anterior (Ant).

Figure 4.10 displays the comparison between the glioma patients in the cohort and the healthy subjects for three left tracts with both FA and peak length as metrics. ATR is the most affected tract based on both FA and peak length, while T PREM and T PAR were determined affected based on the peak length comparison.

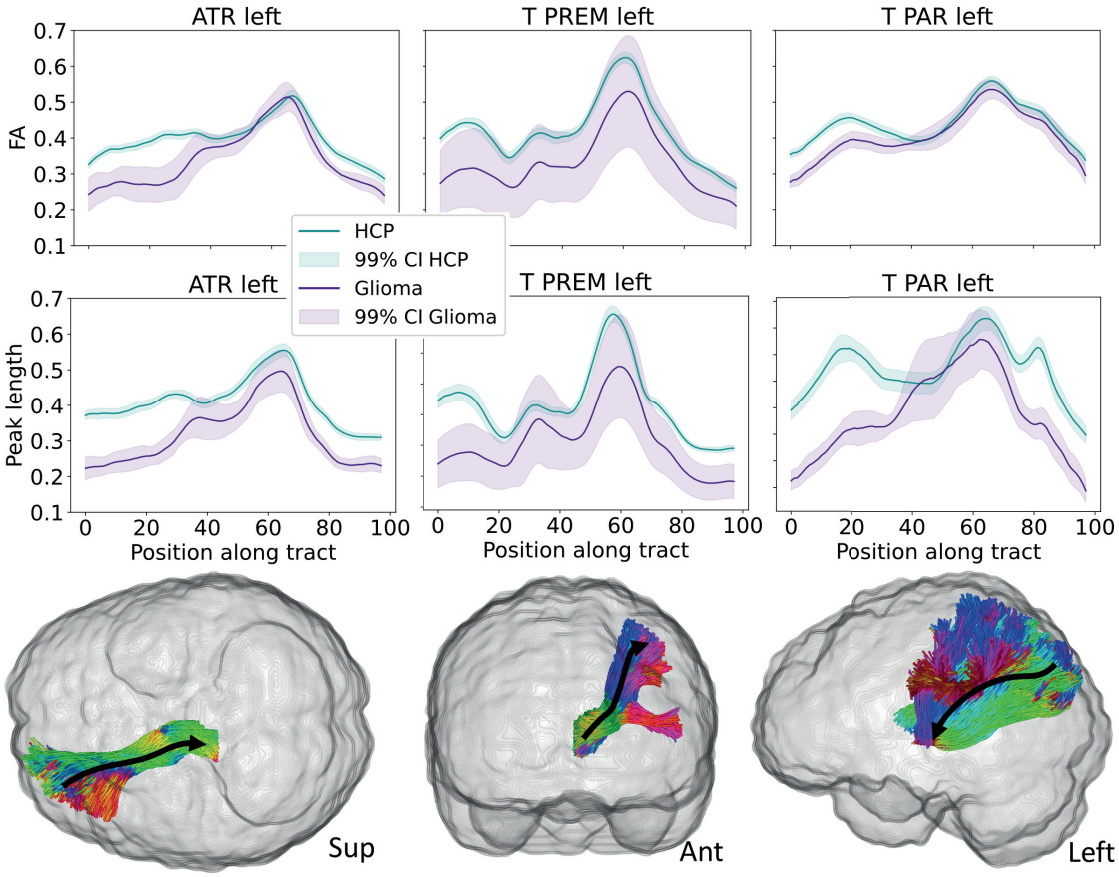

Figure 4.10: Comparison of FA and peak length along the tract profiles of the left anterior thalamic radiation (ATR), left thalamo-premotor (T PREM), and the left thalamo-parietal fascicles (T PAR). 99% confidence intervals are displayed for both the healthy subjects (termed HCP in the figure) and the glioma patients. Visualizations of the tracts are included in the lower part of the figure with the tract profiles drawn, where the views from left to right are: superior (Sup), anterior (Ant), and left.

5

Discussion

The Discussion section of the thesis covers various aspects, including the pre-processing of imaging data for both glioma patients and healthy subjects. It also presents the outcomes of TractSeg analysis on glioma patients, along with a quantitative analysis. Additionally, the section explores potential future research directions.

5.1 Pre-processing of glioma patients' DWI

The pre-processing steps included in the proposed workflow for glioma patients are denoising, removal of Gibbs ringing artifacts, correction of susceptibility-induced distortions, eddy current, motion artifacts, and bias field, followed by registration to MNI and intensity normalization together with the healthy subjects from HCP. These steps and their methods were chosen based on what is commonly done for DWI images according to [20] and a number of articles where TractSeg was implemented [22]–[24], [28], [29]. However, there are many options for pre-processing, such as what parameters or methods to use and which corrections to include, and more testing on the data set at hand is required to find the optimal steps.

Studying the effect of omitting Gibbs ringing removal could lead to more appropriate usage. Specifically, Gibbs ringing artifacts are noticed as fine lines in high contrast areas, and this could not be seen in the DWI images, most likely because of their poor resolution, and it could therefore be argued that it is an unnecessary pre-processing step. Concurring findings were done in a study investigating the influence of pre-processing steps on the sensitivity of DWI to white matter pathology, and it was found that including Gibbs ringing corrections had a negligible impact [67]. Furthermore, it is desired to manipulate the images as little as possible to mitigate the loss of information and hence it could be motivated to have fewer steps in the workflow. On the other hand, according to [20] it is possible that the Gibbs ringing artifacts accumulate when calculating quantitative metrics such as the FA, and the removal of Gibbs ringing artifacts is recommended. To conclude, it is most likely acceptable to include the removal of Gibbs ringing artifacts, but it would be beneficial to study the effect of omitting this step.

5.2 Pre-processing of healthy subjects' DWI

The quantitative analysis of this thesis is based on the comparison between two data sets, 16 glioma patients and 42 healthy subjects. As mentioned under Methods, the acquisition parameters of the DWI images for the two data sets vary a lot, with the glioma patients having a single-shell protocol with b=1000 mm/s^2, while the healthy subjects have a multi-shell protocol with b-values ranging from 5 to 3000 mm/s^2. Different b-values will enable the capture of different types of diffusion, where lower b-values can delineate the diffusion in the blood vessels, and b-values higher than 2000 or 3000 mm/s^2 can capture intra-axonal diffusion. Having very different b-values in the control data set and the glioma patients will make the analysis complicated, and hence the voxel size of the healthy subjects' images was downsampled to that of the glioma patients and only a subset of the volumes was used, namely, the volumes with b-values of 5 and around 1000. Additionally, Figure C.1 in Appendix C displays the effect of changing the different processing steps on the FA values along a tract for the healthy subjects, and a short discussion is included.

The voxel size of the healthy subjects was 1.25 mm^3 and the glioma patients' had 2.33 mm^3, and to make the two data sets comparable, it was necessary to resample them to have the same voxel size. Attempts were made to upsample the glioma patients' DWI images to the voxel size of the healthy subjects, 1.25 mm^3, which also is the voxel size TractSeg is trained on. The immediate effect of upsampling was image files growing larger, leading to computational issues. Moreover, during upsampling the DWI images were interpolated to achieve the new resolution, which does not bring any new information to the image, motivating the observation that the healthy subjects consistently got higher FA than the glioma patients at the voxel size 1.25 mm^3, but not at 2.33 mm^3, leading to the choice of downsampling the healthy subjects' images instead of upsampling the glioma patients' DWI images.

It is complicated to evaluate how appropriate the pre-processing of the healthy subjects images was, but indications of this can be seen in the quantitative comparisons between glioma patients and healthy subjects. For example in Figure 4.4, it can be seen that the left UF follows the average healthy subject FA tract profile quite well without any significant points, and it is also possible to visually confirm that the left UF looks similar to that of the healthy subjects, while the right UF does not. The same can be seen in Figure 4.5 and 4.6, where visually unaffected tracts follow the healthy subjects' profile quite well, indicating that the pre-processing of healthy subjects' images was appropriate.

Another topic with the healthy subjects' data is its registration to MNI, with it being rigidly aligned to the coordinate axes of MNI, and not registered to standard MNI space as the glioma patients' images are. Although this could be a problem if a voxel-by-voxel comparison between healthy subjects and the glioma patients is done, the effects are most likely small since the comparison between glioma patients and healthy subjects is based on metric values along the tract streamlines, which

are computed based on the present white matter structure and not a template or atlas. Therefore, it is only the values along a profile that are compared and not the shapes of the tracts, mitigating the effect of different alignments to MNI.

5.3 TractSeg on glioma patients' DWI

TractSeg is based on three 2D encoder-decoder networks to perform tract segmentation and compute the tract orientation maps for each tract. The networks are trained on healthy subjects where the anatomies follow very similar patterns throughout the data set, as opposed to the potentially very skewed anatomies of glioma patients. A possible issue could arise in the differing anatomies, leading to false segmentations of the tracts. Nevertheless, TractSeg has shown potential in cortico-spinal tract (CST) segmentation for patients with brain pathologies and achieved a higher level of consistency than manual segmentation [55], [56].

Figure 4.3 in Results displays three tracts for two glioma patients where there is a difference between the left and right tracts, but also between glioma and the corresponding tract in the healthy subjects. It can be seen that the left SLF III of glioma patient 1 is bent over the surgical site and was therefore also likely placed around the tumor before resection. Similar reasoning can be done for the displaced right UF of patient 2, which has been compressed towards the anterior due to the tumor. These discoveries and the fact that the tracts were computed without any loss of streamlines shows that TractSeg can handle the skewed anatomies of patients 1 and 2, indicating that TractSeg has the potential to be used to perform tractography on glioma patients, which is in line with other findings in [55], [56]. Future research incorporating a comparison between TractSeg and a manual segmentation method for ground control tract segmentation could be utilized to further establish the performance of TractSeg on glioma patients and skewed anatomies. The manual method does however have inherent limitations in user variability and bias, and the correct ground truth could only be found via dissection, which makes evaluation of TractSeg complicated.

Two final points related to TractSeg's performance are firstly the way TractSeg segments CC 3, making it not symmetrical and a group of streamlines existing inferior to the left, but not to the right, which can be seen in Figure 4.6 with the inferior view having fibers continuing underneath the surgical site, but not in the other direction. Secondly, TractSeg creates tract segmentations that sometimes overlap the ventricles. The diffusion in the ventricles is isotropic, corresponding to low FA values, and this could cause the FA values along the tract profiles to be lower than expected. Although this could be an issue if absolute FA values are compared between studies, as long as TractSeg is used for both data sets in a comparison, the potential error will be the same and can be neglected.

5.4 Quantitative analysis

From the tract-wise FA comparison between each glioma patient and the healthy subjects, three tracts of two glioma patients were included in Figure 4.4, 4.5 and 4.6 in the Results, representing three different cases of how the FA along the tract profile can be affected by the glioma. All these cases have in common that the tract profiles were shorter for the affected tracts in the glioma patients compared to the corresponding tract in the healthy subjects. An important note here is how the tract profiles are constructed since they are determined from the current length of the tract and not a standard length, i.e., if the tract is shorter (e.g., from being cut off by the tumor), the subsequent profile will be shorter and look stretched out compared to the unaltered tract, which will affect the significant point comparison analysis. However, it is still possible to say the FA values along the tract profiles are significantly lower at parts of the affected tracts in the glioma patients.

Figure 4.7 displays full tractograms for two glioma patients, and by studying the T1-weighted anatomical images it is clear that patient 4 had a larger surgical site and skewed anatomy than patient 3. The tractograms further illustrate this since patient 4 has a larger proportion of affected tracts, which were not only in close proximity to the surgical site, but also in other areas of the brain, indicating the impact of the tumor on the patients' brain.

5.4.1 Most affected tracts

The main location of the most affected tracts was the frontal lobe (see Table A.1 in Appendix A for more details on locations of tracts). This is in agreement with the typical tumor locations of low-grade gliomas [5]. These results are however biased to the location of gliomas in the cohort, which do not necessarily represent the general distribution of locations of gliomas. Furthermore, a study distinguished other tracts in the temporal lobe to typically be in close proximity to tumors, such as the left CST, left IFOF, left SLF, and left AF [68]. On the other hand, in this thesis the proximity to the tumor is only indirectly investigated by considering the FA or peak length values along the tract profile, and the specific deviation from healthy patients could have other grounds. For example, it has been seen that gliomas can infiltrate along tracts and spread from the initial tumor, which could affect the tracts in terms of their ability to transmit information [69], and also their plastic ability [5].

The most affected tracts were determined based on the number of glioma patients with more than 20% significant points for each tract. As mentioned under Methods, there is room for improvement in the determination of the most affected tracts. One alternative could be to compute the highest number of significant points by summarizing them for all glioma patients and tracts. However, this would make a very affected tract in one patient have a bigger impact on the determination than a partially affected. Therefore, it was decided to set a threshold level. A low threshold reduced the possibility to distinguish the most affected tract since most tracts for the glioma patients had some significant points, and almost all tracts were shown

to be affected to some extent. A higher level, on the other hand, filtered out glioma patients having parts of their tracts affected, leading to a very low number of glioma patients having any affected tracts. The threshold level of 20% was subsequently chosen. However, the impact of the threshold on which tracts are distinguished to be most affected should be studied to investigate if there is a big variation in the results for different thresholds.

5.4.2 Choice of metric

There is no standard for how tracts are evaluated and compared between subjects, but FA is often considered in articles related to quantitative evaluation and has been thought of as white matter integrity. A decrease in FA could be because of axon degeneration, and it has been seen that FA can be lower in areas with lesions for glioma patients due to loss of structural organization [70]. Additionally, a decreased FA in glioma patients has been connected to a higher level of recurrence [71]. However, since FA depends on a number of factors, such as axon density, membrane permeability, myelination, and the crossing fibers, it is not trivial to associate a decrease in FA with axon degeneration [72].

Using metrics that are not based on the tensor model could potentially overcome some of the limitations of FA and be useful for studying gliomas [16], one being the FOD peak length included in this thesis. The peak length is the norm of the tract orientation maps' (TOM) amplitudes, where the TOMs are tract-specific maps containing one peak of the FOD per voxel. The peak length can therefore handle crossing fibers better than FA since one voxel can contain up to three fiber directions, as opposed to the single direction in the DTI model that underlies the FA. On the other hand, peak length is a measure depending on the accuracy of the TOMs, which means that if peak length should be used as widely as FA, especially for comparison between different studies, it is necessary to have segmentation methods with similar performance. Nevertheless, for within study investigations using TractSeg, peak length is an appropriate option for quantitative comparisons.

Based on Figures 4.8, 4.9, and Figure 4.10 in Results the metrics FA and peak length can be compared for different tracts. For ATR and CC, FA and peak length agrees quite well on both the shape of the profile and how much they differ between the healthy subjects and glioma, although peak length discriminates the right ATR when FA does not. For other tracts such as ST FO and T PAR there is a bigger difference between the shapes of the profiles for the two metrics, with the peak length often differentiating the healthy subjects and glioma patients more than FA does, leading more tracts being classified as affected. This suggests that peak length values differ more between the two data sets than FA does, and to find the reason to this more research is needed.

5.5 Future work

Another potential metric derived from the amplitude of the FOD is called apparent fiber density (AFD) and is more widely employed than the peak length. During high b-values ($> 3000\ s/mm^2$), it can be assumed that the diffusion signal comes from the water inside the axons, since water outside of them is attenuated, and the amplitude of the FOD is proportional to the intra-axonal volume of water, giving a measure of the apparent fiber density. A lower AFD can have many reasons but corresponds to a decreased ability of the tract to transfer information [72]. Unlike FA and the peak length, the AFD has a physiological connection and can be useful for analysis.

The control data, obtained from the Human Connectome Project, has been acquired with a different protocol compared to the glioma patients' data. During future research it is preferable to have control data acquired with the same protocol as the glioma patients to make sure the effects of the glioma on the patient's anatomical properties can be studied and mitigating studying differences based on the different protocols. Indeed, attempts were made to make the data sets more comparable, i.e., by downsampling the healthy subjects' images and selecting which volumes to include based on the corresponding b-value. The attempts made the tracts in areas far from the tumor more similar in terms of FA values, indicating that it was a reasonable choice to adjust the healthy subjects' data.

In this thesis a statistical approach using the Crawford-Howell test and a threshold of 20% significant points to classify a tract as affected for one glioma patient, but there are also other proposed methods for individual or group tract analysis. One method is to study the whole network in the brain by implementing graph theory where certain metrics (FA or peak length for instance) are the weights of the edges that connect the nodes, where the edges represent the tracts and the nodes are nuclei in the gray matter. Subsequently, graph theory specific metrics can be derived and correlated to clinical data. Another suggested method is to employ machine learning to combine multiple metrics from the patients, which could be appropriate for the highly heterogeneous data at hand, and henceforth obtain increased predictive and statistical power [32].

Clinical variables were not included in the thesis and only anonymized images were supplied, and to further evaluate which steps to include in the pre-processing and which metric to use for quantitative evaluation, it is possible to study the correlation between clinical variables and different methodological choices. For example, a potential future study could be to investigate how FA and peak length varies in patients with different types of tumors, and potentially connect that to survivability since it has been seen that glioblastoma patients had decreased survivability if the tumor affected the right ATR, right IFOF, right or left CST, and CC [69]. Another potential study could be to look at the correlation between metrics and neuro-psychological tests, to further delineate the relationship between tract health and patients' quality of life.

Investigations related to possible structural brain plasticity for glioma patients both before and after resection could be done if the proposed pipeline is applied to DWI images of glioma patients acquired before surgery, after the surgery, and long-term follow-up after surgery. Tracts could be compared using FA and peak length and the extent of tract regeneration or increased health could be studied via visual inspection. Additionally, although it is common for gliomas to infiltrate the tracts and therefore potentially reducing the plasticity, low-grade glioma patients provide a unique possibility to study how the brain reacts to slow changes of rearrangement since the tumors often have been growing for many years before the patients experience any symptoms.

6

Conclusions

An automatic image processing workflow to perform tractography for glioma patients using TractSeg was developed and evaluated. TractSeg managed to compute tracts for glioma patients with anatomies differing from the healthy population in 99% of the cases, producing tracts that either went around the surgical site, were narrower, or were interrupted. Further testing with ground control tract outlinings from a manual tractography method is needed to determine the sensitivity of TractSeg for glioma patients' images, but it displays great potential to process the images of the patient group.

Based on the comparison of FA values along tract profiles between healthy subjects and glioma patients, the most affected tracts were the anterior thalamic radiation, corpus callosum and striato-fronto-orbital tract, and based on peak length comparison the thalamic-premotor tract and thalamic-parietal tract were also affected. Most of the affected tracts are in the frontal lobe, which is in line with previous research.

Both FA and peak length can be useful metrics to analyze tracts. It is recommended that future studies include clinical variables and employ the same imaging protocol for both glioma patients and healthy subjects. This approach will facilitate the identification of the most appropriate metric and allow for an in-depth investigation of brain tract health and changes. Furthermore, establishing associations between these factors and patients' cognitive function and quality of life holds the potential to enhance patients' well-being and increase the understanding of the relation between patient cognition and slow changes of white matter in the situation of a brain tumor. These findings could contribute to the overall pursuit of improving the lives of individuals affected by gliomas.

References

[1] M. L. Goodenberger and R. B. Jenkins, "Genetics of adult glioma," *Cancer Genetics*, vol. 205, no. 12, pp. 613–621, Dec. 2012, ISSN: 22107762. DOI: 10.1016/j.cancergen.2012.10.009. [Online]. Available: https://linkinghub.elsevier.com/retrieve/pii/S2210776212002608 (visited on 04/05/2023).

[2] L. Bauchet, "Epidemiology of Diffuse Low Grade Gliomas," in *Diffuse Low-Grade Gliomas in Adults*, H. Duffau, Ed., 2nd ed., Cham: Springer International Publishing, 2017, pp. 13–55, ISBN: 978-3-319-55466-2. DOI: 10.1007/978-3-319-55466-2. [Online]. Available: http://link.springer.com/10.1007/978-3-319-55466-2 (visited on 11/30/2022).

[3] A. Smits and A. S. Jakola, "Clinical Presentation in Diffuse Low-Grade Gliomas," in *Diffuse Low-Grade Gliomas in Adults*, H. Duffau, Ed., Cham: Springer International Publishing, 2017, pp. 199–213, ISBN: 978-3-319-55464-8. DOI: 10.1007/978-3-319-55466-2_11. [Online]. Available: http://link.springer.com/10.1007/978-3-319-55466-2_11 (visited on 01/18/2023).

[4] M. Weller, M. van den Bent, M. Preusser, *et al.*, "EANO guidelines on the diagnosis and treatment of diffuse gliomas of adulthood," *Nature Reviews Clinical Oncology*, vol. 18, no. 3, pp. 170–186, Mar. 2021, ISSN: 1759-4774, 1759-4782. DOI: 10.1038/s41571-020-00447-z. [Online]. Available: https://www.nature.com/articles/s41571-020-00447-z (visited on 01/18/2023).

[5] H. Duffau, Ed., *Diffuse Low-Grade Gliomas in Adults*. Cham: Springer International Publishing, 2017, ISBN: 978-3-319-55466-2. DOI: 10.1007/978-3-319-55466-2. [Online]. Available: http://link.springer.com/10.1007/978-3-319-55466-2 (visited on 11/30/2022).

[6] K. X. Teng, B. Price, S. Joshi, *et al.*, "Life after surgical resection of a low-grade glioma: A prospective cross-sectional study evaluating health-related quality of life," *Journal of Clinical Neuroscience*, vol. 88, pp. 259–267, Jun. 2021, ISSN: 09675868. DOI: 10.1016/j.jocn.2021.03.038. [Online]. Available: https://linkinghub.elsevier.com/retrieve/pii/S096758682100148X (visited on 11/30/2022).

[7] P. Brodal, *The central nervous system: structure and function*, 4th ed. New York: Oxford University Press, 2010, OCLC: ocn426115423, ISBN: 978-0-19-538115-3.

[8] C. M. Filley, *The behavioral neurology of white matter*, 2nd ed. Oxford ; New York: Oxford University Press, 2012, ISBN: 978-0-19-974326-1.

[9] J. Wasserthal, P. F. Neher, D. Hirjak, and K. H. Maier-Hein, "Combined tract segmentation and orientation mapping for bundle-specific tractography," *Medical Image Analysis*, vol. 58, p. 101 559, Dec. 2019, ISSN: 1361-8423. DOI: 10.1016/j.media.2019.101559.

[10] N. Agarwal and J. D. Port, Eds., *Neuroimaging: Anatomy Meets Function*. Cham: Springer International Publishing, 2018, ISBN: 978-3-319-57427-1. DOI: 10.1007/978-3-319-57427-1. [Online]. Available: http://link.springer.com/10.1007/978-3-319-57427-1 (visited on 01/20/2023).

[11] A. Fedorov, R. Beichel, J. Kalpathy-Cramer, *et al.*, "3D Slicer as an image computing platform for the Quantitative Imaging Network," *Magnetic Resonance Imaging*, vol. 30, no. 9, pp. 1323–1341, Nov. 2012, ISSN: 1873-5894. DOI: 10.1016/j.mri.2012.05.001.

[12] J. Wasserthal, P. Neher, and K. H. Maier-Hein, "TractSeg - Fast and accurate white matter tract segmentation," *NeuroImage*, vol. 183, pp. 239–253, Dec. 2018, ISSN: 10538119. DOI: 10.1016/j.neuroimage.2018.07.070. [Online]. Available: https://linkinghub.elsevier.com/retrieve/pii/S1053811918306864 (visited on 01/24/2023).

[13] M. Chappell, *Principles of Medical Imaging for Engineers: From Signals to Images*. Cham: Springer International Publishing, 2019, ISBN: 978-3-030-30511-6. DOI: 10.1007/978-3-030-30511-6. [Online]. Available: http://link.springer.com/10.1007/978-3-030-30511-6 (visited on 02/10/2023).

[14] S. Mori, *Introduction to diffusion tensor imaging*, 1st ed. Amsterdam: Elsevier, 2007, OCLC: 162587824, ISBN: 978-0-444-52828-5.

[15] T. Huisman, "Diffusion-weighted and diffusion tensor imaging of the brain, made easy," *Cancer Imaging*, vol. 10, no. 1A, S163–S171, 2010, ISSN: 14707330. DOI: 10.1102/1470-7330.2010.9023. [Online]. Available: https://www.ncbi.nlm.nih.gov/pmc/articles/PMC2967146/ (visited on 02/06/2023).

[16] F.-C. Yeh, A. Irimia, D. C. d. A. Bastos, and A. J. Golby, "Tractography methods and findings in brain tumors and traumatic brain injury," *NeuroImage*, vol. 245, p. 118 651, Dec. 2021, ISSN: 10538119. DOI: 10.1016/j.neuroimage.2021.118651. [Online]. Available: https://linkinghub.elsevier.com/retrieve/pii/S1053811921009241 (visited on 01/17/2023).

[17] C. Beaulieu, "The basis of anisotropic water diffusion in the nervous system - a technical review," *NMR in biomedicine*, vol. 15, no. 7-8, pp. 435–455, 2002, ISSN: 0952-3480. DOI: 10.1002/nbm.782.

[18] J.-D. Tournier, F. Calamante, and A. Connelly, "Robust determination of the fibre orientation distribution in diffusion MRI: Non-negativity constrained super-resolved spherical deconvolution," *NeuroImage*, vol. 35, no. 4, pp. 1459–1472, May 2007, ISSN: 10538119. DOI: 10.1016/j.neuroimage.2007.02.016. [Online]. Available: https://linkinghub.elsevier.com/retrieve/pii/S1053811907001243 (visited on 02/16/2023).

[19] G. S. Chilla, C. H. Tan, C. Xu, and C. L. Poh, "Diffusion weighted magnetic resonance imaging and its recent trend-a survey," *Quantitative Imaging in Medicine and Surgery*, vol. 5, no. 3, pp. 407–422, Jun. 2015, ISSN: 2223-4292. DOI: 10.3978/j.issn.2223-4292.2015.03.01.

[20] C. M. Tax, M. Bastiani, J. Veraart, E. Garyfallidis, and M. Okan Irfanoglu, "What's new and what's next in diffusion MRI preprocessing," *NeuroImage*, vol. 249, p. 118 830, Apr. 2022, ISSN: 10538119. DOI: 10.1016/j.neuroimage.2021.118830. [Online]. Available: https://linkinghub.elsevier.com/retrieve/pii/S1053811921011010 (visited on 03/23/2023).

[21] J. L. Prince and J. M. Links, *Medical imaging signals and systems*, 2nd ed. Boston: Pearson, 2015, ISBN: 978-0-13-214518-3.

[22] J. Tallus, M. Mohammadian, T. Kurki, T. Roine, J. P. Posti, and O. Tenovuo, "A comparison of diffusion tensor imaging tractography and constrained spherical deconvolution with automatic segmentation in traumatic brain injury," *NeuroImage: Clinical*, vol. 37, p. 103 284, 2022, ISSN: 22131582. DOI: 10.1016/j.nicl.2022.103284. [Online]. Available: https://linkinghub.elsevier.com/retrieve/pii/S2213158222003497 (visited on 01/25/2023).

[23] G. Prasse, H.-J. Meyer, C. Scherlach, *et al.*, "Preoperative language tract integrity is a limiting factor in recovery from aphasia after glioma surgery," *NeuroImage. Clinical*, vol. 37, p. 103 310, Dec. 2022, ISSN: 2213-1582. DOI: 10.1016/j.nicl.2022.103310.

[24] J. Wasserthal, K. H. Maier-Hein, P. F. Neher, *et al.*, "White matter microstructure alterations in cortico-striatal networks are associated with parkinsonism in schizophrenia spectrum disorders," *European Neuropsychopharmacology: The Journal of the European College of Neuropsychopharmacology*, vol. 50, pp. 64–74, Sep. 2021, ISSN: 1873-7862. DOI: 10.1016/j.euroneuro.2021.04.007.

[25] J. L. Andersson, S. Skare, and J. Ashburner, "How to correct susceptibility distortions in spin-echo echo-planar images: Application to diffusion tensor imaging," *NeuroImage*, vol. 20, no. 2, pp. 870–888, Oct. 2003, ISSN: 10538119. DOI: 10.1016/S1053-8119(03)00336-7. [Online]. Available: https://linkinghub.elsevier.com/retrieve/pii/S1053811903003367 (visited on 03/15/2023).

[26] Z. Hou, "A Review on MR Image Intensity Inhomogeneity Correction," *International Journal of Biomedical Imaging*, vol. 2006, pp. 1–11, 2006, ISSN: 1687-4188, 1687-4196. DOI: 10.1155/IJBI/2006/49515. [Online]. Available: http://www.hindawi.com/journals/ijbi/2006/049515/abs/ (visited on 03/16/2023).

[27] J. Juntu, J. Sijbers, D. Dyck, and J. Gielen, "Bias Field Correction for MRI Images," in *Computer Recognition Systems*, M. Kurzyński, E. Puchała, M. Woźniak, and A. Żołnierek, Eds., vol. 30, Series Title: Advances in Soft Computing, Berlin, Heidelberg: Springer Berlin Heidelberg, 2005, pp. 543–551, ISBN: 978-3-540-32390-7. DOI: 10.1007/3-540-32390-2_64. [Online]. Available: http://link.springer.com/10.1007/3-540-32390-2_64 (visited on 03/16/2023).

[28] S. Tu, C. Wang, R. A. L. Menke, *et al.*, "Regional callosal integrity and bilaterality of limb weakness in amyotrophic lateral sclerosis," *Amyotrophic Lateral Sclerosis & Frontotemporal Degeneration*, vol. 21, no. 5-6, pp. 396–402, Aug. 2020, ISSN: 2167-9223. DOI: 10.1080/21678421.2020.1733020.

[29] C. Maher, A. D'Souza, R. Zeng, *et al.*, "White matter alterations in focal to bilateral tonic-clonic seizures," *Frontiers in Neurology*, vol. 13, p. 972 590, 2022, ISSN: 1664-2295. DOI: 10.3389/fneur.2022.972590.

[30] M. Brett, I. S. Johnsrude, and A. M. Owen, "The problem of functional localization in the human brain," *Nature Reviews Neuroscience*, vol. 3, no. 3, pp. 243–249, Mar. 2002, ISSN: 1471-003X, 1471-0048. DOI: 10.1038/nrn756. [Online]. Available: http://www.nature.com/articles/nrn756 (visited on 03/16/2023).

[31] X. Zhang, Y. Feng, W. Chen, *et al.*, "Linear Registration of Brain MRI Using Knowledge-Based Multiple Intermediator Libraries," *Frontiers in Neuroscience*, vol. 13, p. 909, 2019, ISSN: 1662-4548. DOI: 10.3389/fnins.2019.00909.

[32] F. Zhang, A. Daducci, Y. He, *et al.*, "Quantitative mapping of the brain's structural connectivity using diffusion MRI tractography: A review," *NeuroImage*, vol. 249, p. 118 870, Apr. 2022, ISSN: 1095-9572. DOI: 10.1016/j.neuroimage.2021.118870.

[33] E. Mormina, M. Longo, A. Arrigo, *et al.*, "MRI Tractography of Corticospinal Tract and Arcuate Fasciculus in High-Grade Gliomas Performed by Constrained Spherical Deconvolution: Qualitative and Quantitative Analysis," *AJNR. American journal of neuroradiology*, vol. 36, no. 10, pp. 1853–1858, Oct. 2015, ISSN: 1936-959X. DOI: 10.3174/ajnr.A4368.

[34] E. Mormina, A. Arrigo, A. Calamuneri, *et al.*, "Optic radiations evaluation in patients affected by high-grade gliomas: A side-by-side constrained spherical deconvolution and diffusion tensor imaging study," *Neuroradiology*, vol. 58, no. 11, pp. 1067–1075, Nov. 2016, ISSN: 1432-1920. DOI: 10.1007/s00234-016-1732-8.

[35] Z. Sheng, J. Yu, Z. Chen, *et al.*, "Constrained-Spherical Deconvolution Tractography in the Evaluation of the Corticospinal Tract in Glioma Surgery," *Frontiers in Surgery*, vol. 8, p. 646 465, 2021, ISSN: 2296-875X. DOI: 10.3389/fsurg.2021.646465.

[36] Y. Shirazi, M. A. Oghabian, and S. A. H. Batouli, "Along-tract analysis of the white matter is more informative about brain ageing, compared to whole-tract analysis," *Clinical Neurology and Neurosurgery*, vol. 211, p. 107 048, Dec. 2021, ISSN: 1872-6968. DOI: 10.1016/j.clineuro.2021.107048.

[37] J.-D. Tournier, R. Smith, D. Raffelt, *et al.*, "MRtrix3: A fast, flexible and open software framework for medical image processing and visualisation," *NeuroImage*, vol. 202, p. 116 137, Nov. 2019, ISSN: 10538119. DOI: 10.1016/j.neuroimage.2019.116137. [Online]. Available: https://linkinghub.elsevier.com/retrieve/pii/S1053811919307281 (visited on 03/01/2023).

[38] M. W. Woolrich, S. Jbabdi, B. Patenaude, *et al.*, "Bayesian analysis of neuroimaging data in FSL," *NeuroImage*, vol. 45, no. 1 Suppl, S173–186, Mar. 2009, ISSN: 1095-9572. DOI: 10.1016/j.neuroimage.2008.10.055.

[39] S. M. Smith, M. Jenkinson, M. W. Woolrich, *et al.*, "Advances in functional and structural MR image analysis and implementation as FSL," *NeuroImage*, vol. 23 Suppl 1, S208–219, 2004, ISSN: 1053-8119. DOI: 10.1016/j.neuroimage.2004.07.051.

[40] M. Jenkinson, C. F. Beckmann, T. E. J. Behrens, M. W. Woolrich, and S. M. Smith, "FSL," *NeuroImage*, vol. 62, no. 2, pp. 782–790, Aug. 2012, ISSN: 1095-9572. DOI: 10.1016/j.neuroimage.2011.09.015.

[41] E. Garyfallidis, M. Brett, B. Amirbekian, *et al.*, "Dipy, a library for the analysis of diffusion MRI data," *Frontiers in Neuroinformatics*, vol. 8, Feb. 2014, ISSN: 1662-5196. DOI: 10.3389/fninf.2014.00008. [Online]. Available: http://journal.frontiersin.org/article/10.3389/fninf.2014.00008/abstract (visited on 04/19/2023).

[42] J. Veraart, D. S. Novikov, D. Christiaens, B. Ades-aron, J. Sijbers, and E. Fieremans, "Denoising of diffusion MRI using random matrix theory," *NeuroImage*, vol. 142, pp. 394–406, Nov. 2016, ISSN: 10538119. DOI: 10.1016/j.neuroimage.2016.08.016. [Online]. Available: https://linkinghub.elsevier.com/retrieve/pii/S1053811916303949 (visited on 04/19/2023).

[43] J. Veraart, E. Fieremans, and D. S. Novikov, "Diffusion MRI noise mapping using random matrix theory: Diffusion MRI Noise Mapping," *Magnetic Resonance in Medicine*, vol. 76, no. 5, pp. 1582–1593, Nov. 2016, ISSN: 07403194. DOI: 10.1002/mrm.26059. [Online]. Available: https://onlinelibrary.wiley.com/doi/10.1002/mrm.26059 (visited on 04/19/2023).

[44] L. Cordero-Grande, D. Christiaens, J. Hutter, A. N. Price, and J. V. Hajnal, "Complex diffusion-weighted image estimation via matrix recovery under general noise models," *NeuroImage*, vol. 200, pp. 391–404, Oct. 2019, ISSN: 10538119. DOI: 10.1016/j.neuroimage.2019.06.039. [Online]. Available: https://linkinghub.elsevier.com/retrieve/pii/S1053811919305348 (visited on 04/19/2023).

[45] E. Kellner, B. Dhital, V. G. Kiselev, and M. Reisert, "Gibbs-ringing artifact removal based on local subvoxel-shifts," *Magnetic Resonance in Medicine*, vol. 76, no. 5, pp. 1574–1581, Nov. 2016, ISSN: 1522-2594. DOI: 10.1002/mrm.26054.

[46] J. L. R. Andersson and S. N. Sotiropoulos, "An integrated approach to correction for off-resonance effects and subject movement in diffusion MR imaging," *NeuroImage*, vol. 125, pp. 1063–1078, Jan. 2016, ISSN: 1095-9572. DOI: 10.1016/j.neuroimage.2015.10.019.

[47] N. J. Tustison, B. B. Avants, P. A. Cook, *et al.*, "N4ITK: Improved N3 bias correction," *IEEE transactions on medical imaging*, vol. 29, no. 6, pp. 1310–1320, Jun. 2010, ISSN: 1558-254X. DOI: 10.1109/TMI.2010.2046908.

[48] S. M. Smith, "Fast robust automated brain extraction," *Human Brain Mapping*, vol. 17, no. 3, pp. 143–155, Nov. 2002, ISSN: 1065-9471. DOI: 10.1002/hbm.10062.

[49] D. N. Greve and B. Fischl, "Accurate and robust brain image alignment using boundary-based registration," *NeuroImage*, vol. 48, no. 1, pp. 63–72, Oct. 2009, ISSN: 1095-9572. DOI: 10.1016/j.neuroimage.2009.06.060.

[50] M. Jenkinson and S. Smith, "A global optimisation method for robust affine registration of brain images," *Medical Image Analysis*, vol. 5, no. 2, pp. 143–156, Jun. 2001, ISSN: 1361-8415. DOI: 10.1016/s1361-8415(01)00036-6.

[51] M. Jenkinson, P. Bannister, M. Brady, and S. Smith, "Improved optimization for the robust and accurate linear registration and motion correction of brain

images," *NeuroImage*, vol. 17, no. 2, pp. 825–841, Oct. 2002, ISSN: 1053-8119. DOI: 10.1016/s1053-8119(02)91132-8.

[52] J.-D. Tournier, F. Calamante, and A. Connelly, "Determination of the appropriate b value and number of gradient directions for high-angular-resolution diffusion-weighted imaging," *NMR in biomedicine*, vol. 26, no. 12, pp. 1775–1786, Dec. 2013, ISSN: 1099-1492. DOI: 10.1002/nbm.3017.

[53] J.-D. Tournier, F. Calamante, D. G. Gadian, and A. Connelly, "Direct estimation of the fiber orientation density function from diffusion-weighted MRI data using spherical deconvolution," *NeuroImage*, vol. 23, no. 3, pp. 1176–1185, Nov. 2004, ISSN: 1053-8119. DOI: 10.1016/j.neuroimage.2004.07.037.

[54] B. Jeurissen, A. Leemans, J.-D. Tournier, D. K. Jones, and J. Sijbers, "Investigating the prevalence of complex fiber configurations in white matter tissue with diffusion magnetic resonance imaging," *Human Brain Mapping*, vol. 34, no. 11, pp. 2747–2766, Nov. 2013, ISSN: 1097-0193. DOI: 10.1002/hbm.22099.

[55] Y. H. Moshe, D. Ben Bashat, Z. Hananis, M. Teicher, and M. Artzi, "Utilizing the TractSeg Tool for Automatic Corticospinal Tract Segmentation in Patients With Brain Pathology," *Technology in Cancer Research & Treatment*, vol. 21, p. 153 303 382 211 313, Jan. 2022, ISSN: 1533-0346, 1533-0338. DOI: 10.1177/15330338221131387. [Online]. Available: http://journals.sagepub.com/doi/10.1177/15330338221131387 (visited on 02/16/2023).

[56] T. J. Richards, K. L. Anderson, and J. S. Anderson, ""Fully automated segmentation of the corticospinal tract using the TractSeg algorithm in patients with brain tumors"," *Clinical Neurology and Neurosurgery*, vol. 210, p. 107 001, Nov. 2021, ISSN: 03038467. DOI: 10.1016/j.clineuro.2021.107001. [Online]. Available: https://linkinghub.elsevier.com/retrieve/pii/S0303846721005308 (visited on 02/20/2023).

[57] C. Maffei, C. Lee, M. Planich, *et al.*, "Using diffusion MRI data acquired with ultra-high gradient strength to improve tractography in routine-quality data," *NeuroImage*, vol. 245, p. 118 706, Dec. 2021, ISSN: 10538119. DOI: 10.1016/j.neuroimage.2021.118706. [Online]. Available: https://linkinghub.elsevier.com/retrieve/pii/S1053811921009782 (visited on 06/07/2023).

[58] A. Yendiki, "Automated probabilistic reconstruction of white-matter pathways in health and disease using an atlas of the underlying anatomy," *Frontiers in Neuroinformatics*, vol. 5, 2011, ISSN: 16625196. DOI: 10.3389/fninf.2011.00023. [Online]. Available: http://journal.frontiersin.org/article/10.3389/fninf.2011.00023/abstract (visited on 06/07/2023).

[59] E. Garyfallidis, M.-A. Côté, F. Rheault, *et al.*, "Recognition of white matter bundles using local and global streamline-based registration and clustering," *NeuroImage*, vol. 170, pp. 283–295, Apr. 2018, ISSN: 1095-9572. DOI: 10.1016/j.neuroimage.2017.07.015.

[60] M. F. Glasser, S. N. Sotiropoulos, J. A. Wilson, *et al.*, "The minimal preprocessing pipelines for the Human Connectome Project," *NeuroImage*, vol. 80, pp. 105–124, Oct. 2013, ISSN: 1095-9572. DOI: 10.1016/j.neuroimage.2013.04.127.

[61] D. C. Van Essen, K. Ugurbil, E. Auerbach, *et al.*, "The Human Connectome Project: A data acquisition perspective," *NeuroImage*, vol. 62, no. 4, pp. 2222–2231, Oct. 2012, ISSN: 1095-9572. DOI: 10.1016/j.neuroimage.2012.02.018.

[62] J. Xu, S. Moeller, J. Strupp, *et al.*, "Highly Accelerated Whole Brain Imaging Using Aligned-Blipped-Controlled-Aliasing Multiband EPI," vol. 20:2306, Melbourne, Australia, May 2012.

[63] K. Setsompop, B. A. Gagoski, J. R. Polimeni, T. Witzel, V. J. Wedeen, and L. L. Wald, "Blipped-controlled aliasing in parallel imaging for simultaneous multislice echo planar imaging with reduced g-factor penalty," *Magnetic Resonance in Medicine*, vol. 67, no. 5, pp. 1210–1224, May 2012, ISSN: 1522-2594. DOI: 10.1002/mrm.23097.

[64] D. A. Feinberg, S. Moeller, S. M. Smith, *et al.*, "Multiplexed Echo Planar Imaging for Sub-Second Whole Brain FMRI and Fast Diffusion Imaging," *PLoS ONE*, vol. 5, no. 12, P. A. Valdes-Sosa, Ed., e15710, Dec. 2010, ISSN: 1932-6203. DOI: 10.1371/journal.pone.0015710. [Online]. Available: https://dx.plos.org/10.1371/journal.pone.0015710 (visited on 06/08/2023).

[65] B. Q. Chandio, S. L. Risacher, F. Pestilli, *et al.*, "Bundle analytics, a computational framework for investigating the shapes and profiles of brain pathways across populations," *Scientific Reports*, vol. 10, no. 1, p. 17 149, Oct. 2020, ISSN: 2045-2322. DOI: 10.1038/s41598-020-74054-4. [Online]. Available: https://www.nature.com/articles/s41598-020-74054-4 (visited on 04/06/2023).

[66] J. R. Crawford, P. H. Garthwaite, and D. C. Howell, "On comparing a single case with a control sample: An alternative perspective," *Neuropsychologia*, vol. 47, no. 13, pp. 2690–2695, Nov. 2009, ISSN: 1873-3514. DOI: 10.1016/j.neuropsychologia.2009.04.011.

[67] E. N. Kornaropoulos, S. Winzeck, T. Rumetshofer, *et al.*, "Sensitivity of Diffusion MRI to White Matter Pathology: Influence of Diffusion Protocol, Magnetic Field Strength, and Processing Pipeline in Systemic Lupus Erythematosus," *Frontiers in Neurology*, vol. 13, p. 837 385, 2022, ISSN: 1664-2295. DOI: 10.3389/fneur.2022.837385.

[68] T. Gómez Vecchio, A. Neimantaite, A. Corell, *et al.*, "Lower-Grade Gliomas: An Epidemiological Voxel-Based Analysis of Location and Proximity to Eloquent Regions," *Frontiers in Oncology*, vol. 11, p. 748 229, Sep. 2021, ISSN: 2234-943X. DOI: 10.3389/fonc.2021.748229. [Online]. Available: https://www.frontiersin.org/articles/10.3389/fonc.2021.748229/full (visited on 05/25/2023).

[69] J. Wang, L. Yi, Q.-M. Kang, *et al.*, "Glioma invasion along white matter tracts: A dilemma for neurosurgeons," *Cancer Letters*, vol. 526, pp. 103–111, Feb. 2022, ISSN: 1872-7980. DOI: 10.1016/j.canlet.2021.11.020.

[70] H. Duffau, "Lessons from brain mapping in surgery for low-grade glioma: Insights into associations between tumour and brain plasticity," *The Lancet. Neurology*, vol. 4, no. 8, pp. 476–486, Aug. 2005, ISSN: 1474-4422. DOI: 10.1016/S1474-4422(05)70140-X.

[71] S. Bette, T. Huber, J. Gempt, *et al.*, "Local Fractional Anisotropy Is Reduced in Areas with Tumor Recurrence in Glioblastoma," *Radiology*, vol. 283, no. 2, pp. 499–507, May 2017, ISSN: 1527-1315. DOI: 10.1148/radiol.2016152832.

[72] D. Raffelt, J.-D. Tournier, S. Rose, *et al.*, "Apparent Fibre Density: A novel measure for the analysis of diffusion-weighted magnetic resonance images," *NeuroImage*, vol. 59, no. 4, pp. 3976–3994, Feb. 2012, ISSN: 1095-9572. DOI: 10.1016/j.neuroimage.2011.10.045.

Appendix

The Appendix includes a table of the classification of tracts used for this thesis and short comments on their locations, followed by the complete table of affected tracts from the Results of this thesis, and a note on the pre-processing of the healthy subjects' images.

A. Table of all tracts

Table A.1 displays the tracts of the brain and the areas they connect, according to the open-source white matter segmentation tool TractSeg [12].

Table A.1: The 72 tracts in the human brain and their locations are based on the areas they connect according to the classification used in TractSeg.

Fiber/Tract	Location
Association fibers	
Arcuate fascicle (AF)	Broca's area and Wernicke's area.
Cingulum (CG)	Cigulate gyrus and parahippocampal gyrus.
Middle longitudinal fascicle (MLF)	Superior temporal gyrus, parietal and occipital lobe.
Inferior occipito-frontal fascicle (IFOF)	Temporal, frontal, occipital lobe.
Inferior longitudinal fascicle (ILF)	Temporal, occipital lobe.
Superior longitudinal fascicle (SLF) I	Superior parietal and frontal lobe, supplementary motor cortex, premotor cortex.
Superior longitudinal fascicle (SLF) II	Inferior parietal lobe, dorsolateral prefrontal cortex.
Superior longitudinal fascicle (SLF) III	Inferior parietal lobe, premotor, prefrontal cortex.
Uncinate fascicle (UF)	Frontal, temporal lobe.
Projection fibers	
Anterior thalamic radiation (ATR)	Anterior and midline of thalamus, frontal lobe.

Continued on next page

Table A.1 – continued from previous page

Corticospinal tract (CST)	Motor and somatosensory areas in cortex, spinal cord.
Fronto-pontine tract (FPT)	Frontal lobe, pons.
Optic radiation (OR)	Nerves from eyes, visual cortex.
Parieto-occipital pontine (POPT)	Parietal and occipital lobe, pons.
Superior thalamic radiation (STR)	Ventral thalamus, precentral (frontal lobe) and postcentral gyrus (parietal lobe).
Thalamo-precentral (T PREC)	Thalamus, precentral cortex.
Thalamo-prefrontal (T PREF)	Thalamus, prefrontal cortex.
Thalamo-premotor (T PREM)	Thalamus, premotor cortex.
Thalamo-postcentral (T POSTC)	Thalamus, postcentral cortex.
Thalamo-parietal (T PAR)	Thalamus, parietal lobe.
Thalamo-occipital (T OCC)	Thalamus, occipital lobe.
Striato-fronto-orbital (ST FO)	Striatum, orbitofrontal cortex.
Striato-prefrontal (ST PREF)	Striatum, prefrontal cortex.
Striato-premotor (ST PREM)	Striatum, premotor cortex.
Striato-precentral (ST PREC)	Striatum, precentral cortex.
Striato-postcentral (ST POSTC)	Striatum, postcentral cortex.
Striato-parietal (ST PAR)	Striatum, parietal lobe.
Striato-occipital (ST OCC)	Striatum, occipital lobe.
Commissural fibers	
Commissure anterior (CA)	Temporal lobes.
Corpus callosum (CC)	Many areas in the hemispheres.
Rostrum (CC 1)	Frontal lobes.
Genu (CC 2)	Frontal lobes.
Rostral body (CC 3)	Parts of frontal, temporal and parietal lobes.
Anterior midbody (CC 4)	Parietal lobes.
Posterior midbody (CC 5)	Parietal lobes
Isthmus (CC 6)	Parietal lobes.
Splenium (CC 7)	Occipital lobes.
Other fibers	
Fornix (FX)	Out from hippocampus.
Inferior cerebellar peduncle (ICP)	Cerebellum, medulla oblongata, spinal cord.
Middle cerebellar peduncle (MCP)	Cerebellum, pons.
Superior cerebellar peduncle (SCP)	Cerebellum, midbrain.

B. Table of affected tracts

Table B.1 displays the number of patients with more than 20% significant FA and peak length points from the Tractometry comparison for each of the 50 tracts. The number of patients with less than 2000 streamlines (NOS) is also included, indicating that the tract could not be fully computed compared to the healthy subjects from HCP.

Table B.1: Count of patients with affected tracts for FA, peak length, and the number of streamlines (NOS) comparisons.

Tract	FA	Peak length	NOS
AF left	5	7	0
AF right	4	4	0
ATR left	10	16	2
ATR right	9	14	2
CC 1	7	9	1
CC 2	12	14	0
CC 3	11	10	3
CC 4	7	7	1
CC 5	3	1	0
CC 6	6	5	0
CC 7	3	4	0
CG left	7	4	1
CG right	4	5	0
CST left	1	4	0
CST right	1	1	0
FPT left	4	5	0
FPT right	3	3	0
ICP left	0	7	0
ICP right	0	4	0
IFOF left	3	7	1
IFOF right	4	6	1
ILF left	2	5	0
ILF right	3	3	1
MCP	0	0	0
OR left	1	0	0
OR right	1	0	0
POPT left	0	8	0
POPT right	2	4	0
SCP left	0	7	0
SCP right	1	5	0
SLF I left	4	2	0
SLF I right	6	3	0
SLF II left	3	3	1
SLF II right	5	8	0
SLF III left	7	1	0
SLF III right	5	4	1
ST FO left	9	12	0
ST FO right	5	8	1
ST PREM left	4	8	1
ST PREM right	5	7	0
STR left	4	6	0
STR right	1	3	0
T OCC left	7	6	0
T OCC right	2	1	0
T PAR left	4	10	0
T PAR right	6	4	0
T PREM left	5	14	2
T PREM right	5	10	0
UF left	1	1	1
UF right	3	5	0

C. Pre-processing healthy subjects comparison figure

The FA along the left cortico-spinal tract for healthy subjects with different processing steps is presented in Figure C.1, where the healthy subjects' data pre-processed with HCP's minimal processing pipeline is compared to downsampled healthy subjects' images; downsampled and only selected b-values; downsampled, selected b-values, bias field corrected and group intensity normalized. In the figure the healthy subjects are It can be seen that by downsampling the healthy subjects' images, FA values will decrease. A decreased FA from downsampling can be explained by considering the crossing fibers scenario: if there are crossing fibers in a voxel, the ellipsoid that models the diffusion in that voxel will be closer to a sphere than if there are no fibers crossing (this can be further understood by looking at Figure 2.6 in the Theory chapter).

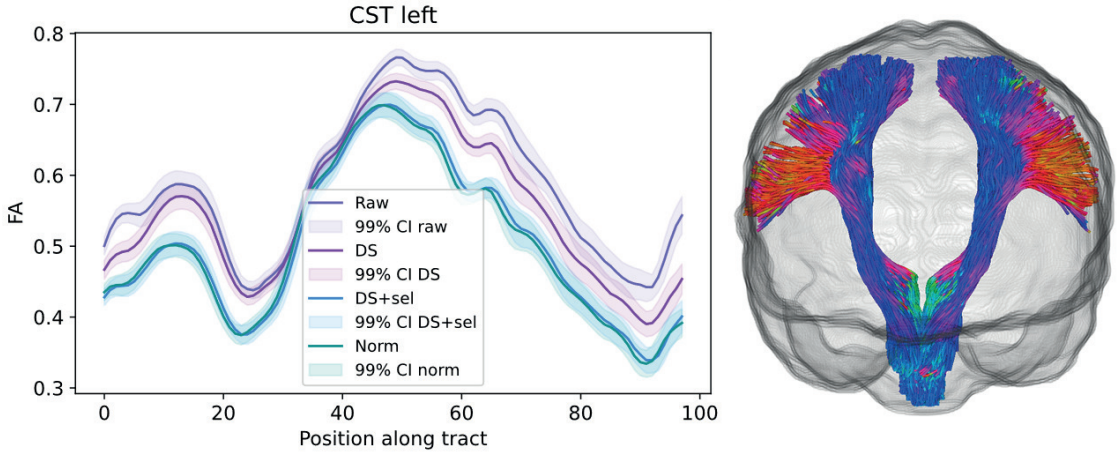

Figure C.1: FA along the cortico-spinal tract for all healthy subjects after performing Tractometry on raw: minimally processed images from humanconnectome.org, DS: downsampled, DS+sel: downsampled and selected b-values, Norm: downsampled, selected b-values, bias field corrected and intensity normalized images.

Only including certain b-values further decreased the FA for the healthy subjects after downsampling. This means that lower b-values cause the ellipsoid to be closer to a sphere and the type of diffusion they inherently capture is more isotropic (i.e., directed) than that of higher b-values. This agrees with the fact that higher b-values are required to study intra-axonal diffusion, which is more anisotropic than diffusion outside of the axons. Finally, it can be seen that the inclusion of bias field correction and intensity normalization did not affect the FA significantly.

DEPARTMENT OF ELECTRICAL ENGINEERING
CHALMERS UNIVERSITY OF TECHNOLOGY
Gothenburg, Sweden 2023
www.chalmers.se

UNIVERSITY OF
GOTHENBURG

CHALMERS
UNIVERSITY OF TECHNOLOGY